$NHSH$ $CR - 165,334$

NASA CR-165334

NASA

NASA-CR-165334

$1981 0016343$

ION SOURCE DESIGN

FOR INDUSTRIAL APPLICATIONS

PREPARED FOR

LEWIS RESEARCH CENTER

NATIONAL AERONAUTICS AND SPACE ADMINISTRATION

GRANT 3086

JUN 2 1981

Final Report

January 1981

Harold R. Kaufman

and

Raymond S. Robinson

Department of Physics
Colorado State University
Fort Collins, Colorado

1. Report No. CR-165334	2. Government Accession No.	3. Recipient's Catalog No.
4. Title and Subtitle ION SOURCE DESIGN FOR INDUSTRIAL APPLICATIONS (U)		5. Report Date January 1981
		6. Performing Organization Code
7. Author(s) Harold R. Kaufman and Raymond S. Robinson		8. Performing Organization Report No.
		10. Work Unit No.
9. Performing Organization Name and Address Department of Physics Colorado State University Fort Collins, Colorado 80523		11. Contract or Grant No. NSG-3086
		13. Type of Report and Period Covered Contract Report
12. Sponsoring Agency Name and Address National Aeronautics and Space Administration Washington, DC 20546		14. Sponsoring Agency Code

15. Supplementary Notes

Grant Manager: Michael J. Mirtich, Jr.
NASA Lewis Research Center
Cleveland, OH 44135

16. Abstract

The design of broad-beam industrial ion sources is described. The approach used emphasizes refractory metal cathodes and permanent-magnet multipole discharge chambers. Design procedures and sample calculations are given for the discharge chamber, ion optics, cathodes, and magnetic circuit. Hardware designs are included for the isolator, cathode supports, anode supports, pole-piece assembly, and ion-optics supports. There are other ways of designing most ion source components, but the designs presented are representative of current technology and adaptable to a wide range of configurations.

17. Key Words (Suggested by Author(s)) Ion Beams Ion Etching Ion Sources Sputtering	18. Distribution Statement Unclassified-Unlimited		
19. Security Classif. (of this report) Unclassified	20. Security Classif. (of this page) Unclassified	21. No. of Pages	22. Price*

N81-24878#

NASA-C-168 (Rev. 10-75)

TABLE OF CONTENTS

I. INTRODUCTION

Broad-beam electron-bombardment ion sources are used for a wide range of industrial applications. There have been a number of reviews of the technology involved,[1-5] in addition to the hundreds of papers upon which these reviews were based. Despite the availability of these publications, applications of this ion source technology have resulted in frequent design problems and much cut-and-try development. The intent of this paper is to cover some of the more frequently used design techniques, together with examples of successful component design. There is no intent of completely covering ion source technology. The intent is, instead, to give at least one specific design example for each component, to aid those that do not have an extensive background of ion source design upon which to draw.

The working gas Ar will be emphasized in performance calculations, although scaling relationships will be given for other gases. The presentation will be divided into sections on the gas feed, discharge chamber, ion optics, cathodes, magnetic design, and mechanical design.

It should be mentioned that single-aperture ion sources have developed almost independently of multiaperture broad-beam sources. Although this paper has been directed primarily at broad-beam sources, much of what is presented is also applicable to single-aperture sources. Where appropriate, single-aperture technology is referenced.

Unless otherwise stated, all equations are in SI (rationalized mks) units. This report is also published as an AIAA paper.[*]

---

[*] H. R. Kaufman and R. S. Robinson, "Ion Source Design for Industrial Applications," _AIAA Paper_ No. 81-0668, April 1981.

II. GAS FEED

The electron-bombardment ion source requires a low pressure gas within the discharge chamber for operation. The gases used in broad-beam ion sources include at least H_2, N_2, Ar, Kr, Xe, Cs, Hg, and CF_4.[4,6,7]

Single-aperture ion-source studies have included a much broader range of gases,[8-10] and should be consulted if more unusual gases are of interest. A direct gas feed has been used with H_2, He, N_2, O_2, F_2, Ne, Cl_2, Ar, Kr. and Xe. Also, the gaseous compounds PH_3, H_2S, AsH_3, H_2Se, SbH_3, H_2Te, BF_3, BCl_3, CO, CO_2, CS_2, SiF_4, PF_5, AsF_3, SbF_3, $SiCl_4$, $GeCl_4$, $AsCl_3$, and $SnCl_4$ have been used in single aperture sources.

If the vapor pressure of the material is too low to use in a direct gas feed, then an external oven or vaporizer can be used. Using this type of feed, single aperture studies have used Li, Na, Mg, P, S, K, Ca, Zn, As, Se, Br_2, Rb, Sr, Cd, In, Sb, Te, I_2, Cs, Ba, Hg, Tl, and Bi, as well as the compounds $BeCl_2$, $AlCl_3$, $MnCl_2$, $FeCl_2$, $SnCl_2$, and $PbCl_4$.

It may appear that the element or compound being vaporized could be placed directly in the ion source, and the ion source heated to produce the proper vapor pressure. With normal ion-source cleanliness, reliable vaporization does not take place below a vapor pressure of roughly 1 Torr. But 1 Torr is decades above the normal operating pressure for an electron-bombardment ion source. The best approach, then, is to use a separate vaporizer that operates at a vapor pressure of 1 Torr, or higher. A flow restriction (orifice, porous plug, or long tube) between the vaporizer and the ion source can be used to reduce the pressure in the discharge chamber to the proper level. All hardware in contact with the gas after the flow restriction should, of course, be hot enough to avoid condensation at the local gas pressure.

The vapor pressure of most materials varies rapidly with temperature, so that accurate control of gas flow from a vaporizer requires a very accurate control of temperature. This temperature control is made more difficult by the conflicting vaporizer requirements of light thermal mass for rapid response and a high degree of temperature uniformity for an unambiguous definition of the vaporizer temperature. In practice, the vaporizer temperature is often used as only a rough indicator of flow, with some other parameter such as extracted beam current used for fine control of vaporizer heating power. Because of these vaporizer problems, if other factors are equal, a normally gaseous material should be chosen over one that requires a vaporizer.

Other feed techniques have been used with single-aperture sources, but are usually quite limited in utility for any sustained operation. For example, a gas of low vapor pressure neutrals can be generated within an ion source by cathode sputtering or by locally heating with a refractory filament. Excess neutral pressure is avoided by condensation of neutrals on the discharge chamber walls. But this condensation also results in rapid depletion of the material supply.

A similar condensation might be expected for low vapor pressure elements from vaporized compounds, due to the fragmentation produced by electron collisions. In practice, other active fragments may recombine with the low vapor pressure elements on the walls almost as fast as they are deposited. Whether or not this recombination takes place will depend on the specific compound involved.

III. DISCHARGE CHAMBER

More complete descriptions of the discharge chamber plasma are available,[3-4] but a short description is included here for convenience. The neutral gas density in the discharge chamber is of the order of 10^{13} cm^{-3} while the electron (and ion) density is roughly a decade lower. The neutrals have a random energy corresponding to the mean wall temperature. The ions are accelerated toward the boundaries to arrive at the latter with approximately the ion acoustic velocity (the minimum required velocity for a steady-state sheath solution),

$$v_a = (e \ T_e/m_i)^{1/2} \ , \tag{1}$$

where e is the absolute electronic charge, T_e is the electron temperature in eV, and m_i is the ion mass. This ion velocity towards boundaries is many times higher than the mean neutral velocity. Thus, although the neutral density is far higher than the ion density, the extraction rate of ions can be equal to, or greater than, the neutral loss rate.

The plasma potential is usually uniform within several volts throughout the discharge chamber, as well as being within several volts of the anode potential. For most applications, it is sufficiently accurate to assume the ions originate at anode potential.

The electrons from the cathode are injected into this plasma with an energy corresponding to approximately the full discharge voltage. They lose energy mostly by exciting or ionizing collisions with neutral atoms. The collisions being with neutrals and with background (Maxwellian) electrons (soft or Coulomb collisions). For initial electron energies greater than about 15-20 eV, the Coulomb cross section is so

small that little energy is lost to background electrons, and the ionizing contribution of the high energy, or primary, electrons is important. These primary electrons make up of the order of 10% of the total electron population, with a low-energy (roughly 1-10 eV) Maxwellian population the remainder.

The mean free path for ionization due to the primary electrons is usually much greater than the discharge chamber dimensions. The containment of these primary electrons is a major design feature of the discharge chamber. This is accomplished by having surfaces at approximately cathode potential so these electrons are reflected, or by having the surfaces protected by a magnetic field that also serves to reflect them. This protection function requires a theoretical magnetic integral between the anode and cathode of

$$\int \vec{B} \times d\vec{x} = 6.74 \times 10^{-6} V_d^{1/2} \; , \tag{2}$$

where the integral is in T-m and the discharge potential difference V_d is in V.

If primary electron containment were the only consideration in choosing a value for the magnetic integral, then a very large value would often be desirable. But the magnetic field also tends to prevent the escape of Maxwellian electrons to the anode, and this escape is required to complete the discharge circuit. The proper selection of magnetic integral is thus a compromise between the value desired for primary electron containment and that desired for Maxwellian electron escape to the anode.

Types of Discharge Chambers

For the most part, two types of discharge chamber are considered in this paper. The first, considered to a lesser extent, is the conventional axial-field chamber shown in Fig 1. This was the first type of discharge chamber used in an electron-bombardment ion source, and is still widely used for small ion sources. For larger sources, though, this type of chamber has serious beam-uniformity problems. These uniformity problems can be partially offset by multiple cathodes.

A much more flexible approach for large ion sources is the multipole type shown in Fig. 2. Because the magnetic field in the multipole type is confined to the region near the wall, the primary electrons have free access to most of the discharge chamber volume, and a uniform plasma can be produced over a large diameter. The multipole approach is also readily adapted to arbitrary discharge-chamber shapes.

The concept of the primary electron region is important in the design-stage prediction of performance. This region is the volume that can be reached directly (without collisions) by primary electrons from the cathode. For the multipole type of chamber, this region is approximately the volume enclosed by the pole pieces, anodes, and ion optics (shown by the dashed line in Fig. 2).

For the axial field design, the best performance is normally obtained using a magnetic field strength at the downstream (toward the ion optics) end of the discharge chamber that is only 60-80% of that at the upstream end. In this case, the primary electron region coincides approximately with the innermost magnetic field line that intercepts the anode, as shown by the dashed line in Fig. 1.
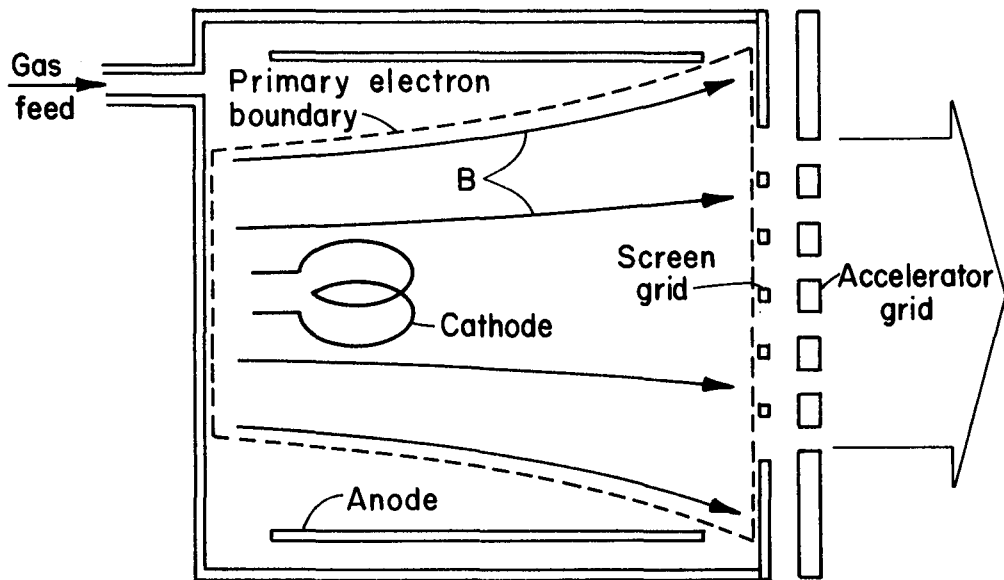
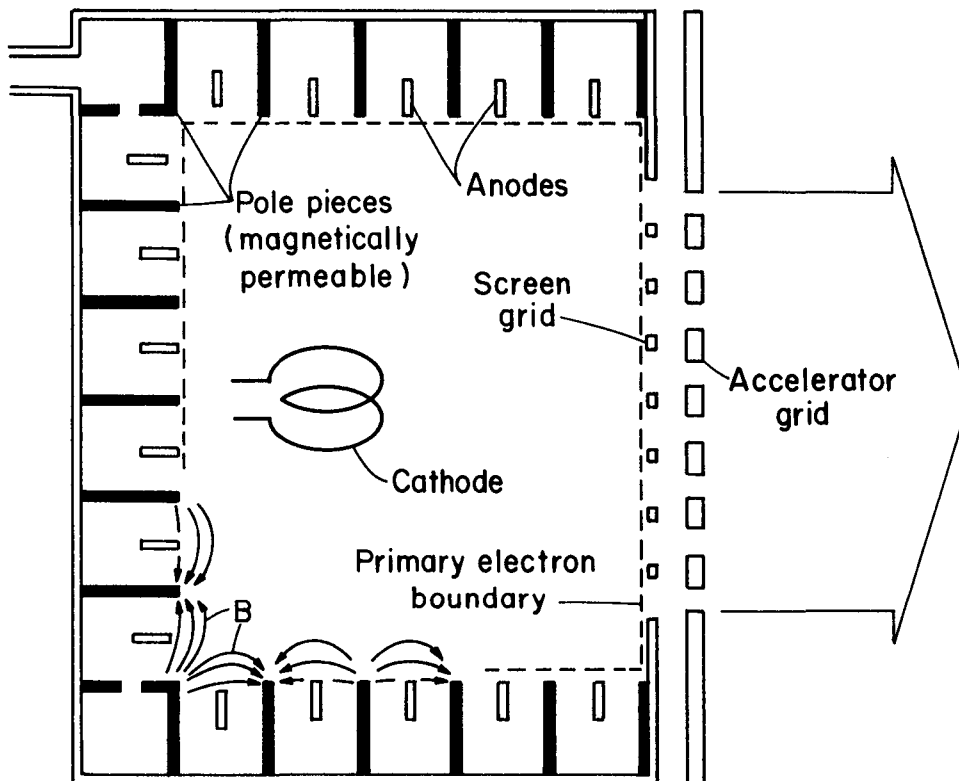Fig. 1. Conventional axial-field discharge chamber.

8

Fig. 2. Multipole discharge chamber. (Magnets between pole pieces not shown.)

Discharge Loss

The ions produced in the discharge chamber tend to go nearly equally in all directions, so that the fraction extracted to form the ion beam should be proportional to the extraction area, A_{ex}, divided by the total outside area of the primary electron region, A_p. If the energy to produce ions is roughly constant for different sources, then this energy, in eV/ion, should be some constant times A_{ex}/A_p. For well designed sources, this is approximately the case, with the discharge energy for Ar being

$$E \sim 50\ A_p/A_{ex}\ . \tag{3}$$

Note that the discharge energy E in eV/ion also equals the discharge power in W per beam A.

The discharge loss of Eq. (3) assumes operation at or near the discharge-loss "knee." As shown in Fig. 3, operation with a low beam current at some discharge-chamber neutral flow rate results in a low discharge loss. As the beam increases, the discharge loss at first rises slowly. After reaching the knee, the discharge loss rises rapidly for a small increase in beam current. If further increases in beam current are desired after reaching the knee, they are best obtained by increasing the neutral flow rate to a higher value, at the same time increasing the discharge power. The normal needs in industrial applications are a high ion beam current and a low background pressure, with the latter obtained at a low neutral flow rate. These conflicting needs are best met with operation at or near the discharge-loss knee.

The discharge loss of Eq. (3) also assumes a properly designed source. The magnetic integral should be about 1.5 times the theoretical
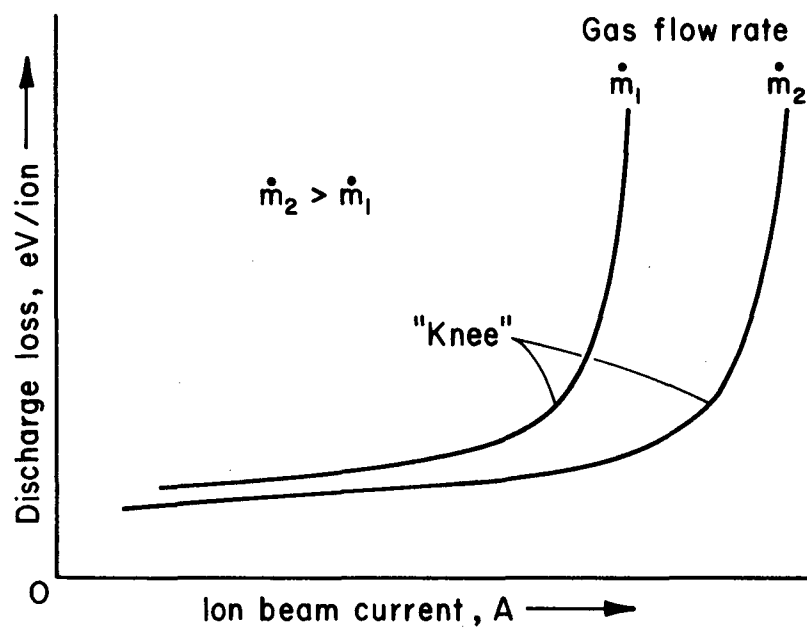
Fig. 3.   Typical variation of discharge loss with extracted ion
beam currents.

value given by Eq. (2). (The decrease in discharge loss is usually small above a factor of about 1.5.) The screen thickness should be roughly 20% of the screen-hole diameter. As mentioned earlier, the downstream magnetic field strength of an axial-field source should be only 60-80% of the upstream value. For this type of source, the cathode should also be located downstream of any magnetic-field maximum. There is some effect of different propellants on the discharge loss, but these effects are generally within about ±30%.

The relative thickness of the screen grid has an important effect on the discharge loss. A semi-empirical equation for this loss variation[4] is

$$E \propto \exp(2t_s/d_s) \ , \tag{4}$$

with the screen thickness t_s and screen-hole diameter d_s as defined in the Ion Optics section. For $t_s/d_s \sim 0$, the constant in Eq. (3) would drop to about 33, while for $t_s/d_s \sim 0.4$, it would rise to about 75.

Within a factor of about 2 (mostly in the increased loss direction) the same method of prediction can be used for discharge losses in single aperture sources. The biggest difficulty usually is the estimation of the primary electron region. Some single-aperture sources resemble the axial-field source of Fig. 1,[11] often without the desirable decrease in field strength in the downstream direction. Others, with a magnetic field transverse to the extraction direction,[12] often have a primary electron region that is only a small fraction of the total discharge-chamber volume.

Neutral Loss

The neutral density at the ion optics, as indicated by the source temperature and the neutral losses through the ion optics, tends toward a constant for similar operation of a particular ion source on one gas. When different ion sources are compared, the density for this similar operation varies with the ratio of primary electron region area, A_p, to primary electron region volume, Ω_p. The analysis of neutral loss was first conducted at the maximum utilization, where the loss curve goes nearly vertical in Fig. 3.[13] As discussed in connection with discharge losses, the knee of the discharge-loss curve is an operating condition of more practical interest. For knee operation and Ar as the gas, the discharge-chamber neutral density is, in m^{-3}, about

$$n_o \sim 1.4\times10^{17}\, A_p/\Omega_p \ , \tag{5}$$

with A_p in m^2 and Ω_p in m^3. For maximum utilization, the neutral density would be about half the value given by Eq. (5). For other monatomic gases, the required neutral density would vary approximately as $1/\sigma m^{1/2}$, and σ the maximum ionization cross section with m the ion mass. For molecular gases, m should be some mean mass including ionized fragments.

The neutral density of Eq. (5) can be given two simple interpretations. One is the external pressure in the vacuum facility that would, in equilibrium, give rise to this density. Assuming an average external temperature of 100°C, an average wall temperature inside the ion source of 400°C, and a gauge calibration temperature of 20°C, the external facility pressure that would produce the required discharge-chamber density would be, in Torr, about

$$P \sim 6\times10^{-6}\ A_p/\Omega_p\ . \tag{6}$$

Note that this calculation assumes some sort of ion gauge that actually measures density. For different gases the pressure given by Eq. (6) should be corrected by the factor $\sigma_{Ar}m_{Ar}^{1/2}/\sigma m^{1/2}$. Because an ion gauge gives a reading roughly proportional to ionization cross section, σ, the uncorrected gauge reading should only require correction by about the ratio $(m_{Ar}/m)^{1/2}$ for other gases. Also note that the pressure given by Eq. (6) assumes that the rate of ion extraction is small compared to the neutral flow rate either in or out. For an ion beam that is significant compared to this neutral flow rate, the deficit due to neutrals being ionized would have to be made up by either a neutral flow direct to the discharge chamber or a higher pressure in the surrounding facility.

The other simple interpretation of the neutral density of Eq. (5) is the neutral loss rate through the ion optics for a zero surrounding facility pressure. Expressed in standard cm^3/sec (at 760 Torr and 20°C), this flow rate would be

$$\dot{N}_o = 0.85\ A_o A_p/\Omega_p\ , \tag{7}$$

where A_o is the equivalent sharp-edged orifice area of the ion optics in m^2 and both A_p and Ω_p are as defined previously. This flow rate again assumes a negligible ion beam. Additional neutral flow will be required in the ratio of 0.249 cm^3/sec for each ampere of beam for a singly ionized monatomic gas such as Ar. The flow rate of Eq. (7) would have to be corrected by a factor $\sigma_{Ar}m_{Ar}/\sigma m$ for gases other than Ar.

The neutral loss theory presented above also can be applied to single-aperture sources. In fact, similar neutral-loss theories were independently developed for single-aperture sources.[14]

The calculation of the equivalent sharp-edged orifice area for the ion optics, A_o, is fairly straightforward. The various ion-optics apertures usually consist of cylindrical sections, where the effective area, A_o, equals the projected open area times a Clausing factor, K_c, that depends on the length-to-diameter ratio of the cylindrical section. The values of K_c for various t/d ratios are given below:[15]

Table 1. Clausing factor.

t/d	K_c	t/d	K_c	t/d	K_c
0.1	0.909	0.6	0.632	1.2	0.471
0.2	0.834	0.7	0.597	1.4	0.436
0.3	0.771	0.8	0.566	1.6	0.406
0.4	0.718	0.9	0.538	1.8	0.381
0.5	0.672	1.0	0.514	2.0	0.359

For ion optics in which the accelerator hole is significantly smaller than the screen hole ($\leq 0.8\, d_s$), it is customary to use only the impedence of the accelerator grid. If $d_a = d_s$, then the usual approach is to ignore the gap (ℓ_g) and simply add the two grid thicknesses to obtain an overall t/d (t/d = $(t_s + t_a)/d_s$). Leakage can be quite important, particularly if the beam extraction dimensions are small compared to the chamber size. If the extracted ion current divided by the neutral loss is to be a high value a thick screen grid is not desirable. The ion recombination loss on the wall of the screen grid hole would then exceed any benefit due to restriction of the neutral flow.[4]

Double Ion Production

For small ion sources at normal operating conditions, the fraction of doubly ionized atoms of a monatomic gas such as Ar can be roughly

estimated from the relative cross sections. Specifically, the fraction
of doubly ionized atoms approximately equals the cross section for
neutral to double ionized divided by the cross section for neutral to
singly ionized, with the energy in eV equal to the discharge potential
difference in V. For Ar, the appearance potential for double ionization
in a single electron collision is about 43 eV. In practice, a 10-15 cm
diameter source will usually have 1-2% doubly charged ions with a 40 V
discharge. For much larger sources, the probability will be significant
that a singly ionized atom will be struck again by an electron before it
escapes from the plasma. To keep the double ion production small for a
very large source, it is necessary to keep the discharge below the
appearance potential for singly ionized atoms to become doubly ionized.[16]

It is often desirable to produce almost all singly ionized atoms in
the ion beam. But it is also often desirable to produce beams with many
doubly ionized atoms. The simple direct approach for the latter is to
use higher discharge voltages. This approach, however, also results in
more sputtering damage. From the preceding discussion, a larger ion
source would also tend to give a higher fraction of double ionized
atoms. Such an approach, though, is often not practical. Assuming
power is not a critical parameter for the initial design, and doubly
(and triply) ionized fraction can usually be increased dramatically by
operating at a high discharge power loss near the minimum neutral loss
point.

To summarize the previous discussion, the doubly ionized fraction
is increased by decreasing neutral pressure or flow and by increasing
discharge voltage and current. The same approaches should also be
effective where fragmentation of a molecule into its constituent atoms
is desired.

Minimum Discharge Voltage

It should be evident from the discussion of double ion production that specific low values of the discharge voltage may be very desirable. It sometimes happens that the discharge cannot be maintained, except at higher voltages. The processes that determine the minimum discharge voltage should be understood, if that voltage is to be modified by design changes.

The minimum discharge voltage that can be sustained is directly related to the density-gradient driven diffusion rate for Maxwellian electrons reaching the anode. To show how the minimum discharge voltage is affected by the electron diffusion, assume that the discharge loss per ion is independent of discharge voltage. (This is approximately true.) Then assume that the discharge current is increased to produce a constant ion beam current as the discharge voltage is reduced. With a constant ion beam current being extracted, the plasma conditions (electron temperature, density, etc.) will also be nearly constant. At some point, in approximate agreement with the Bohm diffusion coefficient for anomalous diffusion, the limit is reached for density-gradient driven diffusion. For any further increase in electron diffusion (and decrease in discharge voltage), the diffusion must be aided by the anode becoming more positive than the bulk of the discharge-chamber plasma. Such an anode potential tends to be unstable in that small disturbances often result in the discharge being extinguished. The limitation in electron diffusion to the anode thus appears as the lower limit on the discharge voltage, with less diffusion capability restricting operation to higher discharge voltages.

The limitation on electron diffusion involves the area for such diffusion as well as the magnetic integral.[16] If the magnetic integral

is ∿1.5 times Eq. (2), the diffusion area for electrons* should typically be 60-70% of the entire primary electron region area, A_p. This amount of diffusion area should permit normal operation with Ar at a discharge voltage at least down to 30-35 V. Although the effect is not a strong one, lighter gases tend to require a greater fraction of A_p for electron diffusion.

Reduction in the minimum permissible discharge voltage with the least impact on an existing design is usually accomplished by reducing the magnetic field strength. The discharge loss in one multipole chamber increased 20-30% when the field integral was reduced from 1.5 to 1.0 times the value given by Eq. (2), so the associated increase in loss can be moderate.

Design Calculation

As a design example, consider a multipole discharge chamber with a primary electron region (dashed line in Fig. 2) that is 10 cm in diameter and 5 cm deep. The major flow restriction to escaping neutrals is an accelerator grid that is 1.0 mm thick with a hexagonal pattern of 1.6 mm diameter holes on 2.5 mm centers over an 8 cm beam diameter. Extraction is through a 0.4 mm thick screen grid with 2.0 mm diameter holes (also on 2.5 mm centers over an 8 cm beam diameter).

The relative screen thickness, t_s/d_s, is 0.4/2 = 0.2. Equation (3) may therefore be used to determine discharge losses at the discharge-loss "knee" (see Fig. 3). The fraction of open area for a hexagonal

---

*For an axial field discharge chamber, the electron diffusion area is approximately the cylindrical wall area. For a multipole chamber, the electron diffusion area is the area occupied by the multipole structure.

array of holes is $0.9069 \times (d_s/\ell_c)^2$, where ℓ_c is the center-to-center spacing. With 2.0 mm holes on 2.5 mm centers, the open area fraction is 0.580. For an 8 cm diameter beam, the extraction area is thus 2.92×10^{-3} m^2. The total outside area of the primary electron region (a 10 cm diameter cylinder, 5 cm long) is 3.14×10^{-2} m^2. The expected discharge loss, from Eq. (3), is $50(0.0314/0.00292) = 540$ eV/ion. For an ion beam current of 0.1 A, for example, a 54 W discharge power would be required. For the further assumption of a 40 V discharge, the discharge current would have to be about 1.4 A.

For the neutral gas loss, the effective open area of the accelerator grid needs to be calculated. With 1.6 mm holes on 2.5 mm centers, the open area fraction is 0.371. For an 8 cm diameter beam, the projected open area is 1.86×10^{-3} m^2. The 1.6 mm diameter holes through a 1.0 mm thick accelerator grid constitute a t/d of 0.625, which corresponds to a Clausing factor K_c of 0.623. Multiplying the projected open area by this Clausing factor gives an equivalent sharp-edged orifice area of 1.16×10^{-3} m^2. The primary electron region area, A_p, has already been calculated as 3.14×10^{-2} m^2. The primary electron region volume (the volume of a cylinder 10 cm in diameter and 5 cm long), Ω_p, is 3.93×10^{-4} m^3. For a vacuum environment in which the backflow of neutrals into the discharge chamber is negligible, Eq. (7) can be used. Substituting for A_o, A_p, and Ω_p yields a neutral loss rate of 0.079 standard cm^3/sec.

If an ion beam of 0.1 A is also to be extracted, an additional 0.025 cm^3/sec is required to supply the atoms for ion extraction (0.249 cm^3/sec for an ampere extracted). The total gas flow to the discharge chamber should therefore be 0.104 cm^3/sec.

Consider next a higher pressure environment, where the discharge-chamber neutral loss is balanced by backflow from the surrounding vacuum chamber. Using Eq. (6), a required chamber pressure of 4.8×10^{-4} Torr is found. If additional backflow is to be supplied for the 0.1 A extracted ion beam, the pressure should be increased by the ratio 0.104/0.079 to $\sim 6.3 \times 10^{-4}$ Torr.

The required gas flow to the discharge chamber is readily calculated for other pressure environments. The backflow varies linearly with chamber pressure, so that interpolation is possible between 0.104 cm^3/sec required at 0 pressure up to no flow required at 6.3×10^{-4} Torr.

Used correctly, calculations similar to those above can be valuable. It should be remembered that these are "knee" calculations, so that it is possible to reduce either discharge losses or neutral losses by increasing the other. It is also necessary to keep in mind that considerable error can be associated with these calculations, often up to a factor of two. The most accurate results will always be obtained when scaling between similar designs using the same propellant. It should also be apparent that multiple ionization and/or fragmentation of molecular propellants can add further complications.

IV. ION OPTICS

The trajectories of ions passing through the optics are determined by the potential distribution in that region, which, in turn, is determined by Poisson's equation. The one-dimensional planar solution for this equation, with zero electric field at the plane of charged-particle origin, is

$$j = (4\varepsilon_o/9)(2q/m)^{1/2}(V^{3/2}/\ell^2) , \qquad (8)$$

where j is the current density of the charged particles, q/m is the charge-to-mass ratio of these particles, V is the potential difference between the plane of origin and any other plane, while ℓ is the distance between those planes.

To obtain an approximation of the current that can be transmitted through a circular aperture of diameter d, the current density of Eq. (8) is multiplied by the area $\pi d^2/4$, giving

$$J = (\pi\varepsilon_o/9)(2q/m)^{1/2}(V^{3/2}d^2/\ell^2) . \qquad (9)$$

For a given q/m and a fixed d/ℓ, J is seen to vary as $V^{3/2}$. For this reason it has been customary to present data in terms of perveance, $J/V^{3/2}$, rather than presenting currents separately for each voltage.

It might be expected from Eq. (9) that the effects of ℓ/d could be incorporated in the perveance using the form of $(J/V^{3/2})(\ell/d)^2$. To date, the best correlation of experimental data and the best agreement with Eq. (9) have been obtained when V is the total voltage V_t, d is the screen hole diameter d_s, and ℓ is the effective acceleration distance ℓ_e.

(See Figs. 4 and 5 for definitions of geometrical and potential parameters.) Making these substitutions in Eq. (9) for Ar^+ ions and rearranging the result,

$$(J/V_t^{3/2})(\ell_e/d_s)^2 = 6.79 \times 10^{-9} . \tag{10}$$

The grouping of parameters on the left in Eq. (10) is called the normalized perveance, and is effective in correlating experimental ion-optics performance. The numerical value on the right is roughly the maximum normalized perveance that can be obtained without excessive accelerator impingement for Ar^+ with $d_a \sim d_s$. For smaller accelerator holes, the maximum normalized perveance would be reduced. For other gases, the current would be expected to vary as $(q/m)^{1/2}$.

The degree of correlation that can be obtained using normalized perveance is indicated in Fig. 6.[17] The data shown were all taken at one value of discharge voltage, V_d, and one value of total accelerating voltage, V_t. Despite the different relative grid spacings, ℓ_g/d_s, and different net-to-total voltage ratios, R, all data show about the same useful ranges for normalized perveance. The right end of each curve was limited by excessive impingement, but all curves end in the range of 3.4-3.6×10^{-9} $A/V^{3/2}$. The solid portion of each curve shows the normalized perveance where the half-angle of beam divergence was within 10% of the minimum value for that combination of ℓ_g/d_s and R. The right ends of the solid curves are in the range 3.1-3.4×10^{-9} $A/V^{3/2}$, while the left ends are in the range 1.5-1.9×10^{-9} $A/V^{3/2}$. In comparison, the use of perveance (not normalized) would introduce a difference factor between maximum and minimum ℓ_g/d_s (through ℓ_e/d_s) of over 2.5.
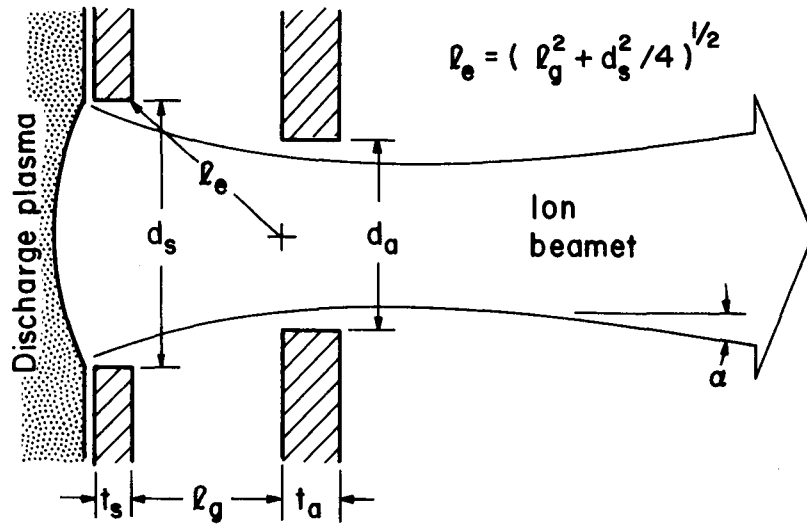
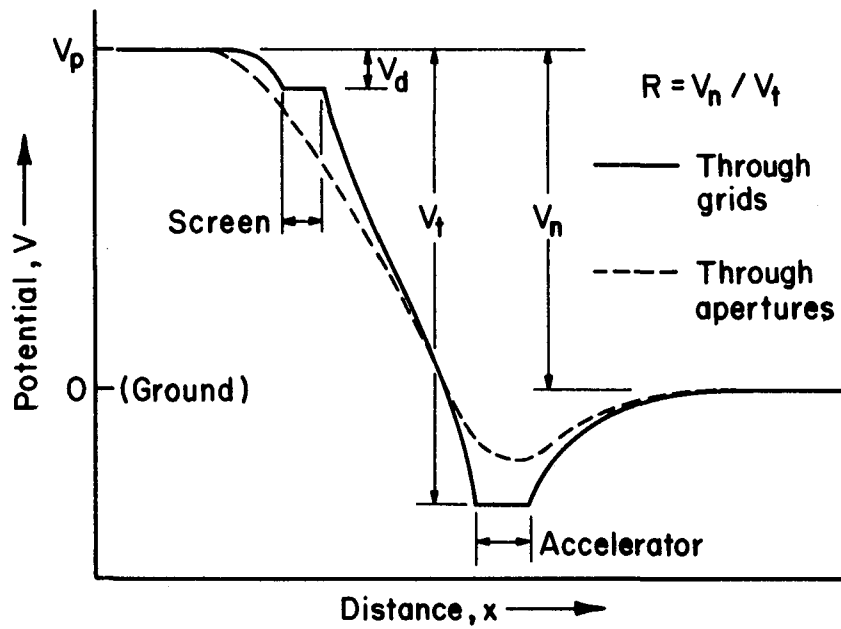Fig. 4. Geometrical parameters for two-grid ion optics.

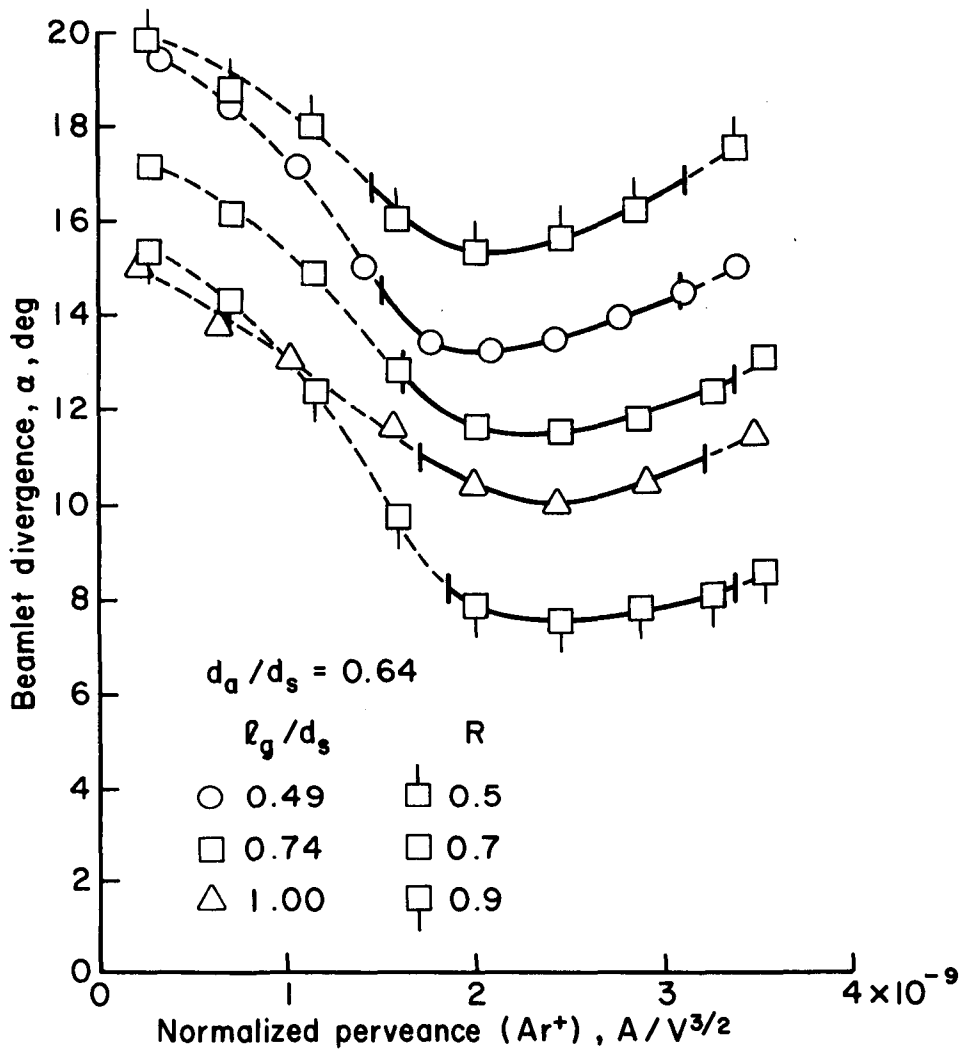Fig. 5. Potential parameters for two-grid ion optics.

Fig. 6. Variation of ion-beam divergence with operating conditions,
using normalized perveance as a correlating parameter.
(Two-grid ion optics, V_d/V_t = constant.)

The use of normalized perveance thus facilitates the comparison of performance over a wide range of operating conditions.

Two-Grid Optics

Two-grid optics imply a potential variation similar to that shown in Fig. 5, with the screen grid close to discharge plasma potential, V_p, and the accelerator grid negative relative to ground. The screen grid is usually at cathode potential, so that it is less than plasma potential by the discharge voltage, V_d. The accelerator must be negative of ground by a value at least sufficient to make the potential in the center of the accelerator aperture equal to that of ground. Otherwise electron backstreaming can occur from the neutralized ion beam, giving a false indication of ion beam current and raising the beam potential in the process. With R the net-to-total voltage ratio (see Fig. 5), the maximum value of R that can be used without encountering electron back-streaming is

$$(1-R_{max}) \ell_e/d_a \sim 0.2 \exp(-t_a/d_a) . \tag{11}$$

This equation has a semiempirical derivation,[4] but appears to agree well with experimental observation.

The data shown in Fig. 6 were obtained with two-grid optics. These data indicate that the normalized perveance range for best focusing and the maximum normalized perveance (limited by accelerator grid impingement) are both substantially independent of ℓ_g/d_s and R.

The data of Fig. 6, as mentioned, were obtained at constant values of discharge voltage, V_d, and total voltage, V_t. There is an effect on performance if the ratio of these voltages is not constant. The data

shown in Fig. 7 indicate a clear trend toward higher normalized perveance as the ratio V_d/V_t is decreased.[18-20] The cause for this effect is believed due to the relative effect of V_d on the plasma sheath near the screen hole. The screen is customarily at cathode potential, so that the discharge plasma is positive relative to the screen by about V_d. With other voltages held constant, increasing V_d causes the sheath near the edge of a screen grid hole to recede into the discharge chamber. To retain the same degree of focusing with this sheath displacement at the edge of the hole, it is necessary to let the sheath also recede at the center of the screen hole. The latter movement is accomplished by reducing the plasma density, and hence the extracted ion current. Thus, for similar focusing, it is necessary to operate at a lower perveance as V_d is increased relative to V_t.

The explanation given above is consistent with the relative location of the theory points in Fig. 7. These points were obtained from digital computer solutions in which the discharge plasma was assumed to be at the same potential as the screen grid ($V_d = 0$).

The region of best focusing has been discussed in some detail, but the degree of focusing obtained is also important. The minimum angle of divergence is shown in Fig. 8 as a function of ℓ_g/d_s and R.[17,18] The effect of V_d/V_r on this minimum angle appears small and within the possible experimental error for most of the range of variables, with the difference at $\ell_g/d_s = 1.0$ and R = 1.0 being a possible exception. Note that the divergence angle α is actually a half-angle from the axial direction. Also, the minimum values in Fig. 8 were the reference values for the 10% increase referred to in Fig. 7.

From the data shown in Fig. 8, a further improvement in focusing would be expected for values of $\ell_g/d_s > 1$. Such values have not been
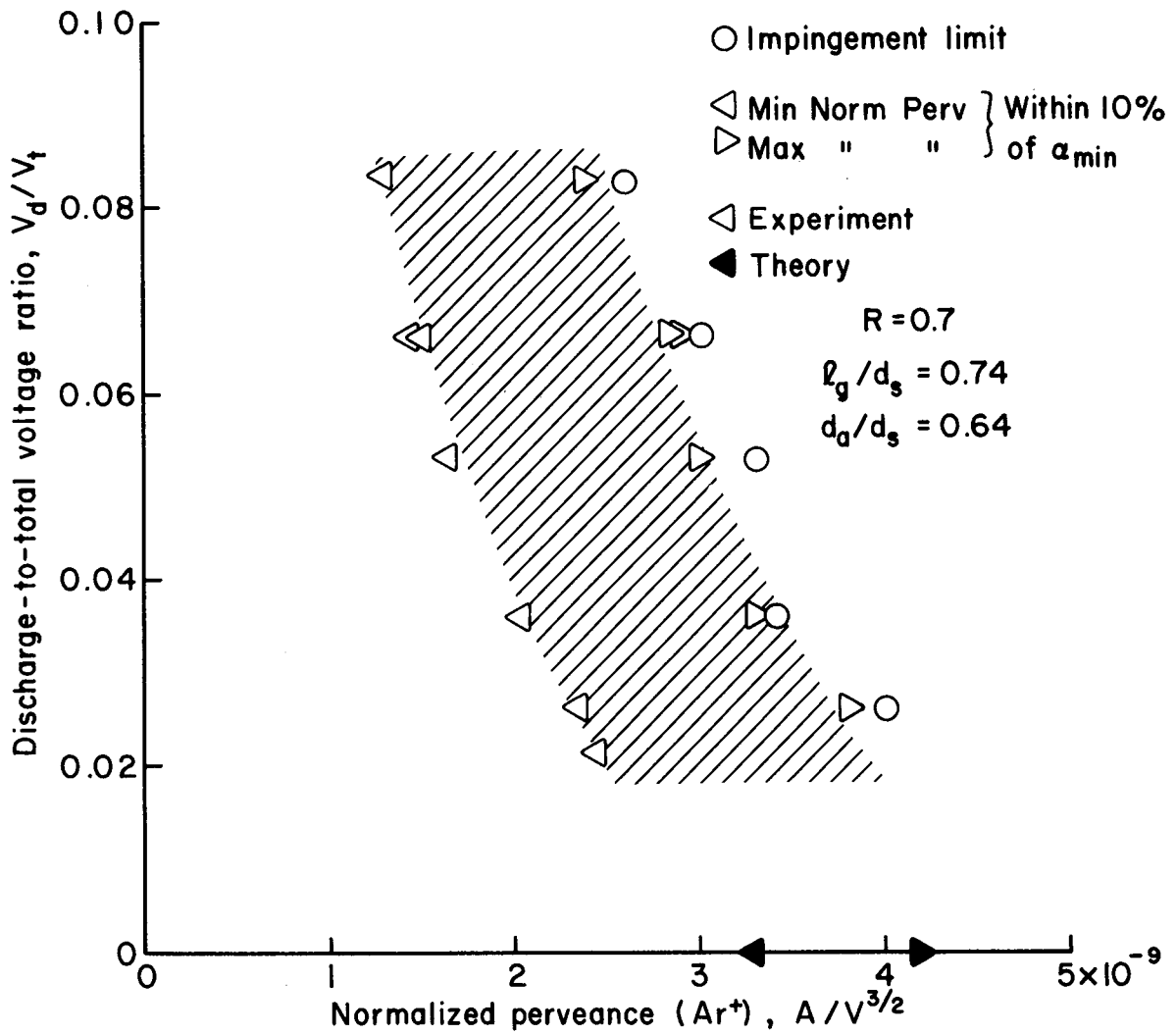
Fig. 7. Effect of discharge-to-total voltage ratio on normalized-perveance operating range for two-grid optics.
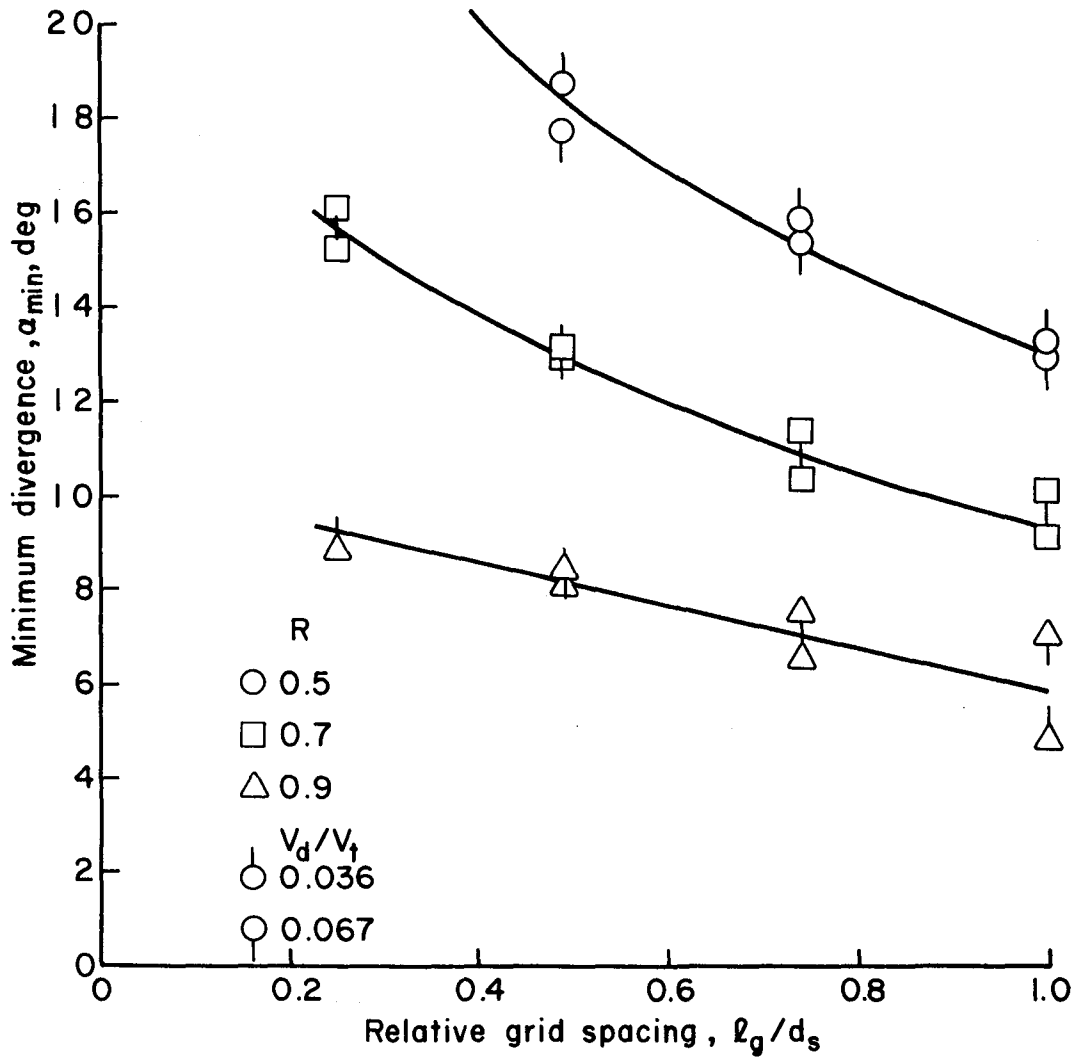
Fig. 8. Effect of relative grid spacing on minimum ion-beam divergence for two-grid optics.

investigated as part of the studies referenced above, but were evaluated as part of the fusion injection program.[21,22] Care should be used in comparing the two sets of data, though. The angles used for Fig. 8 are the values that enclosed 95% of the beam current. The values used most in the fusion injection program include Gaussian half width[21] and rms deviation.[22]

The only major parametric effect left undescribed is that of the relative accelerator hole diameter, d_a/d_s. Experimental data[17] are shown in Fig. 9 for only one value of V_d/V_t, 0.067. Theoretical results[19,20] in Fig. 9 show a clear qualitative agreement with experimental data, but displaced to higher normalized perveances. Much of the perveance difference can be attributed to the difference in V_d/V_t (see Fig. 7). But detailed comparisons suggest that the experimental beamlet diameter (from a single grid hole) was actually larger and less focused than indicated by the digital computer solutions at comparable operating conditions. Some of the difference between theoretical and experimental appears to result from this difference in beamlet diameter.

The best method for calculating the effect of accelerator hole diameter appears to be to use Fig. 7 for the maximum normalized perveance at $d_a/d_s = 0.64$. Then the slope of Fig. 9 ($\sim 8 \times 10^7$) can be used to correct to other values of d_a/d_s.

Two parameters do not have a significant effect on focusing or maximum perveance. Up to a value of about 0.25, the relative screen grid thickness, t_s/d_s, has little effect. In a similar manner, the relative accelerator grid thickness, t_a/d_s, has little effect up to a value of at least 0.4.

All dimensions in the preceding discussion have been given in terms of dimensionless ratios (d_a/d_s, ℓ_g/d_s, etc.). This approach can be
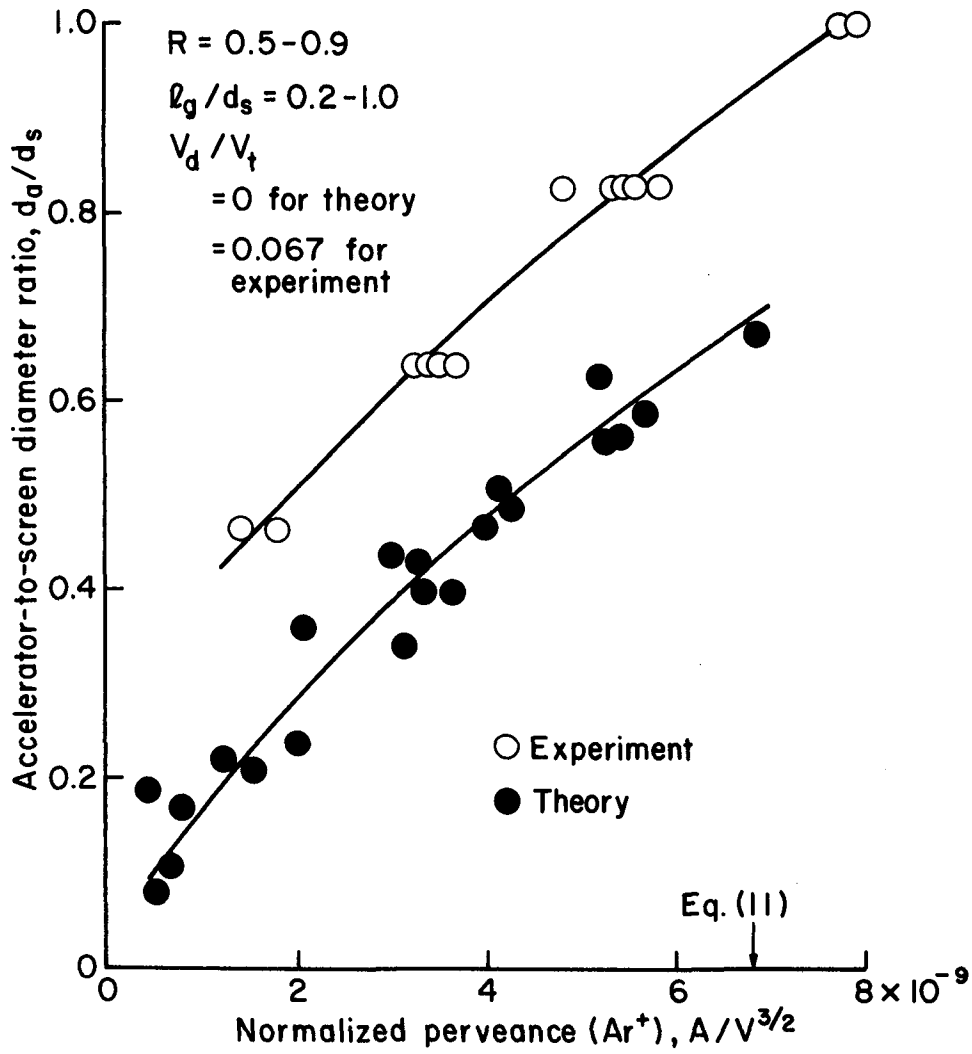
Fig. 9. Effect of accelerator hole diameter on maximum
perveance for two-grid optics.

justified from theoretical results (such as Eqs. (9) and (10), for example) in that only ratios of dimensions can be shown to have any significance. In practice, the absolute dimensions appear to have little importance for d_s > 2 mm. For smaller values of d_s, the maximum normalized perveance is substantially decreased. The reason for this effect is not clear, but it has been verified in independent investigations.[4,18] It is still possible to gain in current density by going to values of d_s < 2 mm, because the increase in hole density can more than offset the decreased capability of each hole. But operation with d_s < 2 mm should be considered as uncertain in any new design, because of the absence of a thorough understanding of this effect. For a design estimate, one set of data indicates a decrease in maximum normalized perveance roughly in proportion to d_s below 2 mm.[18]

Three-Grid Optics

For three-grid optics, a third or decelerator grid is assumed to be downstream of the accelerator and to be at ground potential. The spacing of this decelerator grid from the accelerator is ℓ_d, while the hole diameter and thickness for this grid are d_d and t_d.

The electron backstreaming limit can be adversely affected by the presence of the decelerator grid, but Eq. (11) should still give at least a rough estimate of the limit to be expected.[19,20] In practice, the operating range of most interest for three-grid optics is usually at low values of R, far from the backstreaming limit.

With the additional dimensions involved in the third grid, one might expect a much more complex picture than was presented for two-grid optics. Practical considerations, however, greatly simplify this picture.

The added complexity of three-grid optics can be justified only if better performance can be obtained. The better performance is found in the excellent focusing that can be obtained at low R values. But this excellent focusing is obtained in only a narrow range of normalized perveance. Not surprisingly, this range of normalized perveance is essentially the same as the range for best focusing with two-grid optics. The relative accelerator hole diameter, d_a/d_s, of 0.64 was thus found to be effective for three-grid optics.[23,24] Because the beamlet tends to spread out after passing through the accelerator, a relative decelerator hole diameter, d_d/d_s, of 0.8 was found to be a good choice. Other accelerator and decelerator dimensions were tried, but did not show as much focusing advantage over two grid optics. The relative accelerator and decelerator thicknesses, t_a/d_s and t_d/d_s, were both 0.37 for the tests described below, but the effects on focusing should be minor for values from 0 to 0.4.

Figure 10 shows the improved focusing possible with three-grid optics. Using three grids, the minimum beam divergence is far less at R = 0.3 than was shown in Fig. 8 for R = 0.5 and the same values of ℓ_g/d_s. If two-grid data were available for the same R value, the difference would be even greater.

Using the same 10% increase in beam divergence from the minimum value to define operating range, Fig. 11 was constructed. For the range of variables shown, the operating range does not differ significantly from the two-grid operating range for the same value of V_d/V_t, which is shown by the shaded region.

It should be noted that no $\ell_g/d_s = \ell_d/d_s = 1.0$ points are included in Fig. 10. This large spacing resulted in a drastic reduction of the operating range to about 2.5–2.9 × 10^{-9}. No data were obtained for
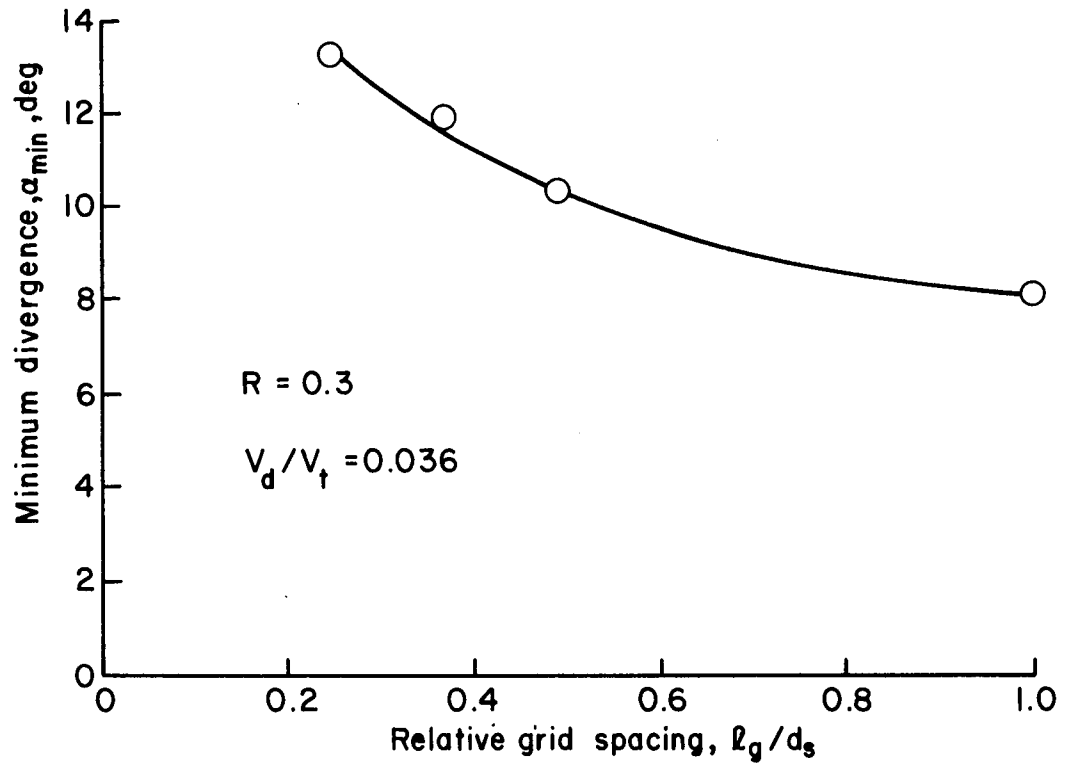
Fig. 10. Effect of relative grid spacing on minimum ion-beam
divergence for three-grid optics. (Decelerator spacing
ℓ_d equal to accelerator spacing ℓ_g.)
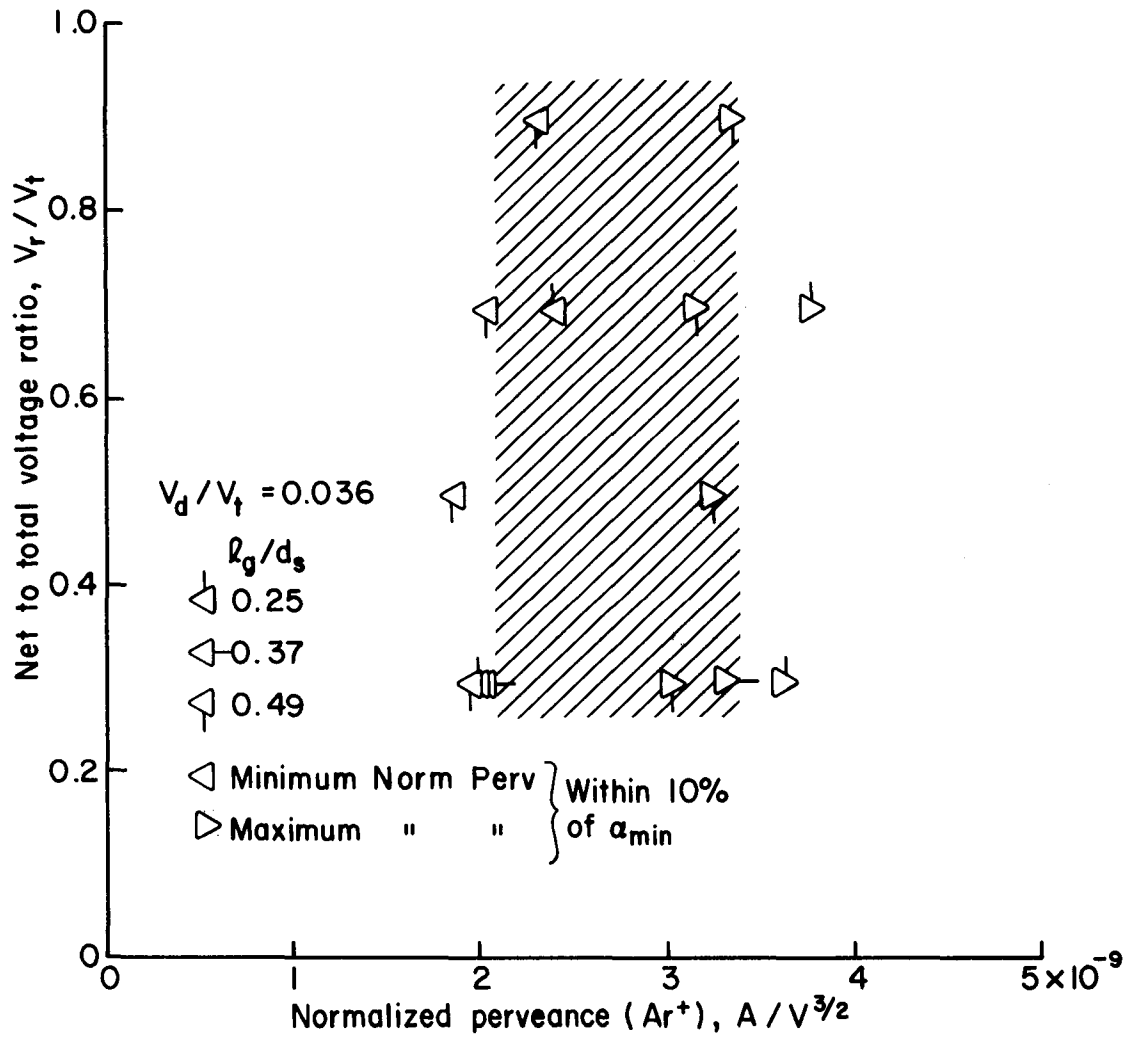
Fig. 11. Normalized-perveance operating range for three-grid
optics. (Decelerator spacing ℓ_d equal to accelerator
spacing ℓ_g.)

relative spacings between 0.49 and 1.00, so it is not possible to state where the reduction in operating range occurs.

An additional improvement in focusing can be obtained by reducing ℓ_d/d_s below the value of ℓ_g/d_s. This approach should be considered where span-to-gap ratio is not a limit. The simultaneous reduction of ℓ_d/d_s and t_a/d_s was not investigated, but may show additional focusing benefits, because the value of t_a/d_s generally used (0.37) was substantial compared to the range of interest for ℓ_d/d_s.

Design Values

The design of ion optics can involve substantial uncertainties. Where possible, designs should be conservative by a margin of 20%, or more, depending on the particular problems involved. The uncertainties should be kept in mind when using the information in this section.

Ignoring grid spacings for a moment, it is possible to cover most broad-beam ion-optics applications with a limited number of designs. These designs will be called: High-collimation two-grid (Design I), High-perveance two-grid (Design II), and Three-grid (Design III). For Design I, $d_a/d_s = 0.64$. For Design II, $d_a/d_s = 0.8-1.0$. For Design III, $d_a/d_s = 0.64$ and $d_d/d_s = 0.80$. The relative thicknesses t_a/d_s and t_d/d_s will be ≤ 0.4. The major effect of the relative screen thickness is on discharge loss and is discussed in the Discharge Chamber section.

The operating range for normalized perveance (left side in Eq. (10)) is shown in the following table for Designs I and III.

Table 2. Normalized perveance (Ar^+) operating range for
Designs I and III.

V_d/V_t	$d_a/d_s = 0.64$
0.02	$2.5\text{--}3.8 \times 10^{-9}$ $A/V^{3/2}$
0.04	$2.0\text{--}3.3 \times 10^{-9}$
0.06	$1.6\text{--}2.9 \times 10^{-9}$
0.08	$1.3\text{--}2.6 \times 10^{-9}$

These ranges were obtained from Figs. 7 and assume a beam divergence
within 10% of the minimum for the ℓ_g/d_s (and ℓ_d/d_s, if three-grid) that
is used.

For Design II, the slope of Fig. 9 was used to correct from a d_a/d_s
of 0.64 to larger values. This correction can be expressed as

$$\Delta N.P. = 1.2 \times 10^{-8} \, \Delta d_a/d_s \quad (Ar^+) \tag{12}$$

With this correction, the approximate maximum normalized perveances for
Design II were:

Table 3. Maximum normalized perveance (Ar^+) for Design II.

V_d/V_t	$d_a/d_s = 0.8$	$d_a/d_s = 1.0$
0.02	5.7×10^{-9} $A/V^{3/2}$	8.1×10^{-9} $A/V^{3/2}$
0.04	5.2×10^{-9}	7.6×10^{-9}
0.06	4.8×10^{-9}	7.2×10^{-9}
0.08	4.5×10^{-9}	6.9×10^{-9}

As a sample calculation, we can assume V_d = 40 V and ℓ_g/d_s = 0.50, with Ar^+ ions. We could interpolate and extrapolate for other values of V_d/V_t, but only the results for 0.02, 0.04, 0.06, and 0.08 will be given. With these assumptions, the maximum currents per hole for Designs I, II, and III are about:

Table 4. Current per hole for various designs (ℓ_g/d_s = 0.5).

| V_d/V_t | V_t | Designs I & III | Design II | |
			d_a/d_s = 0.8	d_a/d_s = 1.0
0.02	2000V	680. µA	1020. µA	1449. µA
0.04	1000V	209.	329.	481.
0.06	667V	99.8	165.	248.
0.08	500V	58.1	101.	154.

For other gases, these currents would be corrected by the factor $(q/m)^{1/2}$, as indicated by Eqs. (8) and (9). For example, Xe^+ with an atomic weight of 131.3, instead of Ar^+ with 39.95, would give only 55.2% of the currents shown.

The minimum divergence, α_{min}, is shown in the following table for two-grid optics:

Table 5. Minimum beam divergence for Designs I and II.

ℓ_g/d_s	R = 0.5	R = 0.7	R = 0.9
0.25	25.2* deg	15.6 deg	8.8* deg
0.49	18.3	13.1	8.2
0.74	15.6	10.9	7.1
1.00	13.2	9.6	5.9

*Data available only for V_d/F_t = 0.036.

Except where noted, the divergence values given are the averages for V_d/V_t of 0.036 and 0.067. In the absence of any additional data, these average values should probably be used for all values of V_d/V_t. The value of α_{min} does not change significantly for values of $d_a/d_s > 0.64$, but the beam divergence at maximum perveance will increase. For $d_a/d_s = 0.8$ the beam divergence will increase up to about 4 deg at maximum perveance, while for $d_a/d_s = 1.0$ it will increase up to about 8 deg.

The minimum divergence, α_{min}, is shown in the following table for three-grid optics with $\ell_d = \ell_g$:

Table 6. Minimum beam divergence for Design III.

ℓ_g/d_s	R = 0.3	R = 0.5	R = 0.7	R = 0.9
0.25	13.3 deg	–	8.0 deg	–
0.49	10.3	8.1 deg	7.2	6.0 deg

As for the preceding two-grid table, these divergences are recommended for all values of V_d/V_t. The divergences for $\ell_g/d_s = 0.49$ were also measured with a reduced value of $\ell_d/d_s = 0.25$, giving 8.0, 6.9, 6.7, and 6.0 deg for R values of 0.3, 0.5, 0.7, and 0.9. At a further reduction to $\ell_d/d_s = 0.12$ the divergences were 7.6 and 6.5 deg at R values of 0.3 and 0.5.

The design procedure often consists of maximizing ion beam current for a given ion energy and a maximum acceptable beam divergence. When a design (I, II, or III) is found that will meet the divergence requirement at some operating condition, the current per hole can be maximized by reducing ℓ_g/d_s and R until the divergence requirement is just met. It may be necessary to try a number of combinations of ℓ_g/d_s and R, but

the trial-and-error procedure for maximizing beamlet current is fairly straightforward. If more than one design will meet the maximum divergence requirement, all should be separately optimized and then compared.

To translate the current per hole into an average current density requires consideration of several limits. At low voltages, for example, it is often found that the screen holes should be as small as possible to permit more holes per unit beam area. As mentioned earlier, the screen hole diameter should not be reduced below 2 mm without also reducing the expected current per hole. Even then, it should be kept in mind that there is limited understanding of operation with smaller screen holes.

Another limit that must be considered is the maximum permissible electric field. The best information on maximum electric field has been obtained with Hg as the working gas,[4] where a value of about 2 kV/mm (V_t/ℓ_g) was found for large gaps, with possibly higher fields acceptable for gaps less than 1 mm. In the absence of any specific information for Ar, this same limit of 2 kV/mm has been used. The reader should keep in mind that, in addition to the uncertainty of the maximum field for various gases, there is the uncertainty in the limit itself. The breakdown limit of 2 kV/mm represents the approximate limit imposed by frequent arcing between the screen and accelerator grids after prolonged operation. If highly polished, much higher fields can be sustained until the polished finish is degraded - sometimes by arcing. (This approach has been used in the fusion injection program.) If only conventional machining has been used, a gradual conditioning of several hours may be required to reach 2 kV/mm. This gradual conditioning may also be required if the ion optics have been exposed to the atmosphere for days or weeks.

One may find that, in the course of reducing the size of the ion optics to obtain more holes per unit beam area, this reduction is limited by the maximum permissible electric field. If the screen hole is still larger than 2 mm, there may be a current-density advantage in reducing the screen hole diameter to 2 mm while keeping ℓ_g at the minimum value. This advantage results from the current per hole being a function of the effective acceleration distance, ℓ_e, while the maximum electric field is a function of ℓ_g. A further increase in current density may then be obtained by decreasing R slightly, to offset the improved focusing that results from the increased ℓ_g/d_s.

Another limit that must be considered is that of the minimum stable and predictable value of ℓ_g. This may result from machining tolerances, but more often is associated with the span-to-gap limit in broad-beam ion optics. The span-to-gap limit will be discussed further in the Mechanical Design section.

The focusing of a broad ion beam by the systematic deflection of beamlets may be of interest to either increase the current density at a target, or to increase the target area that is uniformly covered (defocusing). There are two techniques that are frequently used to accomplish the deflection of beamlets. One is to use spherically dished grids and to align apertures along radial lines. This technique is straightforward and can be used to obtain large increases in current density on small targets or, conversely, large increases in target area covered at the same target distance. In either case the problem is resolved by geometrical considerations that are almost self evident.[25]

The other frequently used technique for deflecting beamlets is aperture displacement. If an accelerator aperture is displaced in one direction (normal to the ion velocity), the beamlet will be deflected in

the opposite direction. The amount of deflection that can be obtained

in this manner is limited by beamlet impingement on the side of the

accelerator hole. In practice, this maximum deflection is roughly equal

to the beamlet divergence angle α. The theory of beamlet deflection by

aperture displacement has been tested and is readily available for

application.[25] The small magnitude of the maximum possible deflection

has limited the use of the aperture-displacement technique in industrial

applications.

A type of optimization that is often encountered is maximizing the

ratio of extracted ion current to neutral loss. For a large extracted

ion current, a large accelerator hole diameter is desired. But to

reduce neutral losses, small accelerator holes are desired. To resolve

this apparent conflict, it is necessary to examine experimental data.

It is, of course, necessary to use a large number of small screen holes

to increase the extracted current. For the same reason the gap ℓ_g

should be as small as possible consistent with focusing, electric field,

and span-to-gap limits. Assuming that these parts of the optimization

are handled correctly, though, what should be the value of d_a/d_s? The

answer to this question is found by plotting the ratio of normalized

perveance divided by $K_c(d_a/d_s)^2$, where K_c is the Clausing factor given

in Table 1. For reasonable assumptions of accelerator thickness, the

above ratio usually optimizes close to a value of 0.64 for d_a/d_s.

Since this is also a value consistent with small divergence angles, it

will usually be a satisfactory final choice. Design II should therefore

also be considered when the ratio of ion current to neutral loss is to

be maximized.

V. CATHODES

Refractory metal cathodes are widely used and represent the present technology level. Other means of emitting electrons will clearly be of increasing interest in the future,[5] but only refractory cathodes will be discussed herein.

Discharge-Chamber Cathode

The optimum operating condition for a discharge-chamber cathode will depend on the exact environment involved. From experience, though, a reasonable place to start in cathode optimization is at an electron emission current density of about 1 A/cm^2. The following table was calculated for this current density and a range of wire sizes using available information on Ta and W:[26]

Table 7. Filament emitter properties for emission density of 1 A/cm^2.

Wire dia,	mm	0.25	0.38	0.51	0.64	0.76
	in	0.010	0.015	0.020	0.025	0.030
Emission,	A/cm	0.08	0.12	0.16	0.20	0.24
Ta (2480°K)	A	5.1	9.4	14.4	20.1	26.5
	V/cm	0.08	0.77	0.67	0.60	0.54
W (2640°K)	A	6.7	12.3	19.0	26.6	34.9
	V/cm	1.03	0.84	0.73	0.65	0.59

With nonreactive gases, W has the advantage of not sagging at high temperatures, but becomes very brittle after use. In contrast, Ta retains good ductility after use, but sags when cantilever shapes are heated. For nonreactive gases the lifetime should be several tens of hours at $V_d \sim 40$ V for a cathode wire diameter of 0.25 mm. The lifetime should increase nearly proportional to the wire diameter when larger

sizes are used. Careful control of contaminants can increase the lifetime substantially, while additional contaminants can greatly reduce it. (Contaminants include gases and backsputtered materials from targets in sputtering applications.) If the contamination level is low, cathode lifetime is determined primarily by sputtering erosion due to ions. This means that cathode lifetime is strongly dependent on the discharge voltage.

Reactive gases can reduce the lifetime of a 0.25 mm cathode to an hour or so. Using a mixture of inert and reactive gases will give added lifetime if 100% reactive gas is not required. Ta and W often show different sensitivities to contaminants and reactive gases, so that it may be desirable to try both.

As a short example of using the previous table, consider the use of 0.25 mm Ta wire to emit 1.0 A of electrons. From the emission/cm (0.080), 12.5 cm of length will be required. If the cathode is to be a single segment, a heating current of 5.1 A is indicated. For 12.5 cm of length, the voltage should be $12.5 \times 0.94 = 11.75$. Because of tolerance variations in wire diameter, a current of at least 6 A should be available from the heater power supply, even if no other wire size will ever be used. To allow for contact resistances and lead losses, 15-20 V should be available. If a very short cathode segment is to be used, remember that there is little emission for several mm near cathode supports due to cooling effects.

Neutralizer Cathode

The emission capability is usually not a significant parameter for the neutralizer. Instead, the current limitation due to the space-charge effect is much more important.

The space-charge effect for a neutralizer can be approximated with electrons only between the neutralizer and a virtual anode located at a radius r from the neutralizer, such that the electron density there equals the background ion density.[*] For equal charge density at this radius, it is necessary that

$$j_e/j_i = (m_i V_c/m_e V_n)^{1/2} \tag{13}$$

where j_e is the electron current density at the radius r, j_i is the local ion current density, m_i is the ion mass, m_e is the electron mass, V_c is the neutralizer-to-beam coupling voltage, and V_n is the net voltage through which the ions have been accelerated. The electron current density of Eq. (13) can also be expressed as an electron emission per unit neutralizer length,

$$J_e/\ell_n = 2\pi r j_i (m_i V_c/m_e V_n)^{1/2} . \tag{14}$$

For a neutralizer with a radius that is small compared to the virtual anode radius,[**] r, the emission per unit neutralizer length is[27]

$$J_e/\ell_n = (8\pi\varepsilon_o/9)(2q/m_e)^{1/2} V_c^{3/2}/r . \tag{15}$$

---

[*]Outside of this virtual anode, the initial velocity of the electrons should be rapidly randomized as the result of two-stream instability.

[**]This assumption is only roughly true, but the following neutralizer calculation is only intended to be approximate.

It may be interesting to the reader that calculating this current as a density over the area $2\pi\ell_n r$ results in a very close resemblance between this radial flow equation and Child's law, Eq. (8). Equating the two expressions for J_e/ℓ_n and solving for r,

$$r = (2\varepsilon_o^{1/2}/3)(2q/m_i)^{1/4}V_c^{1/2}V_n^{1/4}/j_1^{1/2} \tag{16}$$

With numerical values of the various constants substituted and the ion mass expressed in amu (atomic mass units) per electronic charge,

$$r = 2.338\times10^{-4}V_c^{1/2}V_n^{1/4}/j_i^{1/2}m_i^{1/4} , \tag{17}$$

$$J_e/\ell_n = 268.3\, rj_i(m_iV_c/V_n)^{1/2} . \tag{18}$$

These equations should be used by substituting specific values for V_c, V_n, j_i, and m_i into Eq. (17). Then these same values, together with the value of r obtained, are substituted into Eq. (18) to obtain J_e/ℓ_n.

As a specific example in the use of these equations, let the ion beam be 500 eV Ar^+ ions (39.95 amu) at 1 mA/cm^2 (10 A/m^2). With these values substituted, Eqs. (17) and (18) become

$$r = 1.391\times10^{-4}\, V_c^{1/2} , \tag{19}$$

$$J_e/\ell_n = 758.4\, rV_c^{1/2} . \tag{20}$$

The results are tabulated below for a range of assumed coupling voltages, V_c:

Table 8. Neutralizing coupling parameters for 1 mA/cm^2 of 500 eV Ar$^+$ ions.

V_c, V	5	10	20	50	100
r, mm	0.31	0.44	0.62	0.98	1.39
J_e/ℓ_n, A/cm	0.005	0.011	0.021	0.053	0.105

If a total electron neutralization current of 0.1 A is necessary, a coupling voltage of 5 V would require a neutralizer length of about 20 cm, while 10 V would require a length of about 9 cm. The voltage drop along the neutralizer due to the heating current should be included in any evaluation. If necessary, a numerical integration can be performed along the neutralizer. It frequently occurs that almost all the neutralizer emission comes from only a part of the total neutralizer length near the negative end.

Note that the emission per unit length in the preceding table is less than what would be expected for 1 A/cm^2 from a 0.25 mm wire, except for a coupling voltage of 100 V. This means, if a low coupling voltage is desired, that the neutralizer length is usually more important than the diameter. Since sputtering contamination of the neutralizer will increase directly with the projected area struck by electrons, a thin neutralizer is the preferred configuration for low contamination.

The lifetime of a neutralizer in nonreactive gases is determined primarily by sputtering. For a 1-2 mA/cm^2 beam of 500 eV Ar$^+$ ions, one should expect 10-20 hours of life. Lifetime should decrease with an increase in ion energy, but at less than a linear rate. Because of the sputtering erosion mechanism, life will increase with a neutralizer diameter increase, but so will contamination, as discussed above.

As with the main cathode, reactive gases can drastically reduce neutralizer lifetime.

A neutralizer immersed in the ion beam was assumed for these calculations. If the neutralizer is placed outside of the ion beam, in the surrounding charge-exchange plasma,[28] the coupling becomes much more of a problem. In general, an immersed neutralizer is needed to neutralize a broad ion beam. If the beam is directed against a conductor so that current neutralization is not required, or if the beam is a low current one at high energy, then it may be possible to couple adequately from a neutralizer outside of the ion beam. Otherwise, use of an external refractory cathode will usually result in coupling voltages of several hundred to several thousand volts.

VI. MAGNETIC DESIGN

A permanent magnet design is usually simpler, cheaper, and more reliable than an electromagnet design. The preferred type of permanent magnet is usually Alnico V because it is readily available, has a high demagnetization temperature, and has worked well in many past designs.

Permanent Magnets

The demagnetization curve for a permanent magnet material is indicated in Fig. 12, with the demagnetization following the solid line in the direction indicated by the arrows. If the demagnetization process is reversed, the recovery will follow different paths as indicated by the dashed lines. For normal ion source design, the magnet is more demagnetized in an isolated state than it is when installed between permeable pole pieces. So the left ends of the dashed lines should correspond to isolated magnets. For Alnico V a length-to-diameter ratio of 4:1, when isolated, would correspond to about the left end of the upper dashed line, with little permanent loss in flux density due to demagnetization. A smaller length-to-diameter ratio would correspond to a lower dashed line with a greater permanent loss.

For the calculations herein, a flux density of 1.0 tesla will be assumed for an Alnico V magnet with a length-to-diameter ratio of ≥4:1, whether isolated or installed between pole pieces. For shorter magnets than 4:1, the flux density should be reduced in proportion to the length-to-diameter ratio.

Actual flux densities can be expected to vary from the above approximate values. To keep the variation from being even greater, the handling of the permanent magnets should be carefully controlled after magnetization.
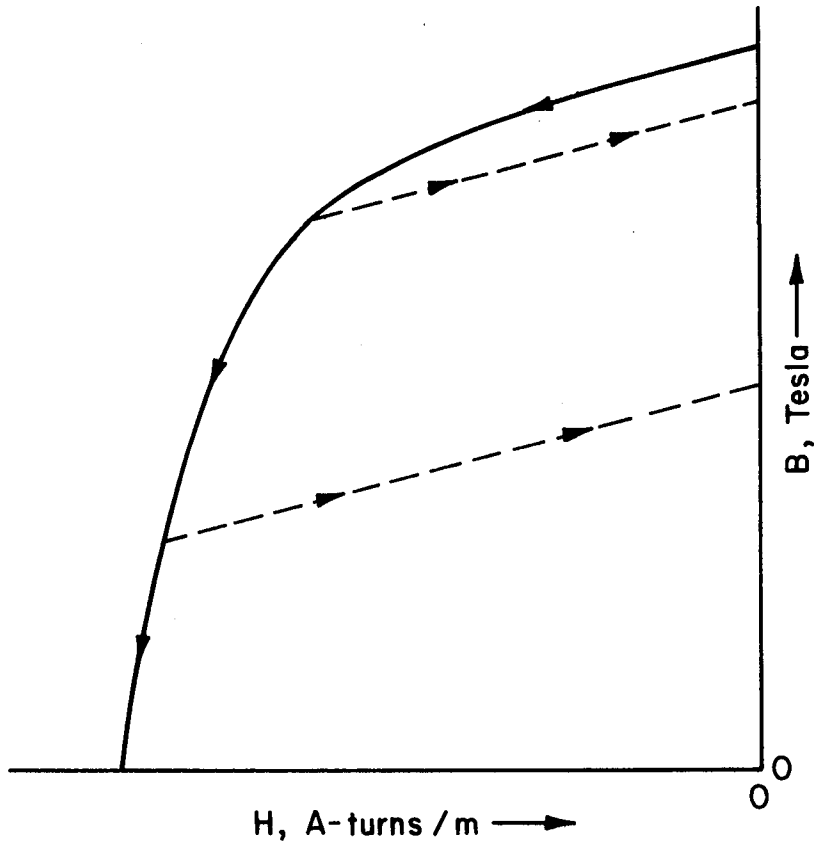
Fig. 12.   Demagnetization curve for permanent magnet (solid line).

Pole Pieces

The usual design approach is to have permanent magnets extend between permeable pole pieces, which are made of mild (low-carbon) steel. If corrosion resistance is a concern for the pole pieces, 400 series stainless steel (ferromagnetic) should be considered.

As indicated in the discussion of the permanent magnets, the flux through the magnets does not vary significantly with the pole-piece design. The total flux can therefore be calculated directly from the total cross section of the magnets used. Also, the permeability of the pole pieces is quite high, so that the magnetic impedance of the pole pieces can be ignored compared to that of the air (or vacuum) gap. The latter can be assured to be approximately true by avoiding saturation. To this end, the average flux density at any section should not exceed about 1 Tesla. Because the maximum flux density is usually found where the magnet contacts the pole piece, this is the region to check against the 1 Tesla value. With 1 Tesla within the magnet, this 1 Tesla condition is met by making the pole piece thickness at that location equal to at least one-fourth of the permanent magnet diameter.

For purposes of design, the pole pieces will be assumed to be parallel, thin, and separated by magnets. The magnetic field shape between two such pole pieces is indicated in Fig. 13(a). For the purposes of calculation, an assumed equivalent field shape will be used, shown in Fig. 13(b). In the equivalent, the field is assumed to have a uniform strength throughout the gap, but the pole pieces are assumed to extend an additional distance Δw in all directions. This distance Δw is related to the spacing between pole pieces, t,

$$\Delta w = K t , \qquad\qquad (21)$$
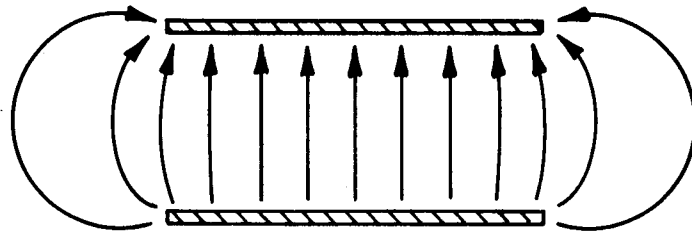
(a) Actual
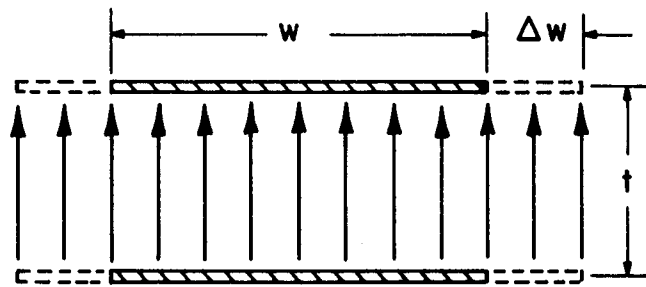
(b) Assumed equivalent

Fig. 13. Magnetic field shape between pole pieces.

with K a constant depending on pole piece configuration. Figure 14 shows several typical pole-piece configurations and the associated values for K. The value of K for two isolated parallel pole pieces of equal size, Fig. 14(a), is well known from potential-field studies as approximately 0.5. When one of two isolated pole pieces is much larger than the other, Fig. 14(b), the value of K is 1.0. (With a little reflection, it should be evident that the potential solution for Fig. 14(b) is equivalent to half that for Fig. 14(a). The factor of two in K follows directly from this equivalence.) For closely spaced pole pieces, in either radial or axial configurations as indicated in Figs. 14(c) and (d), K is about 0.2. This value of 0.2 has been approximately determined by a number of hardware tests, but has not yet been supported by more fundamental potential-field studies.

The configurations shown in Figs. 14 (c) and (d) imply that there is no difference between the value of K for end pairs of pole pieces and the value of K for pairs far removed from the end. For an end pair, with field interference on only one side, a value midway between 0.3 and 0.5 might be expected. Tests to date have not been very precise, but indicate that K should be closer to 0.3 than 0.5. For this reason, no distinction is made between the end pair of a long array of poles and other pairs.

Another special case concerns the corner pole pieces, where the cylindrical wall of the discharge chamber meets the back wall. The added interference of this corner location has been taken care of by recessing the corner anodes, by an amount equal to 10% of the pole piece spacing. This recessed anode location has been indicated in Fig. 2.
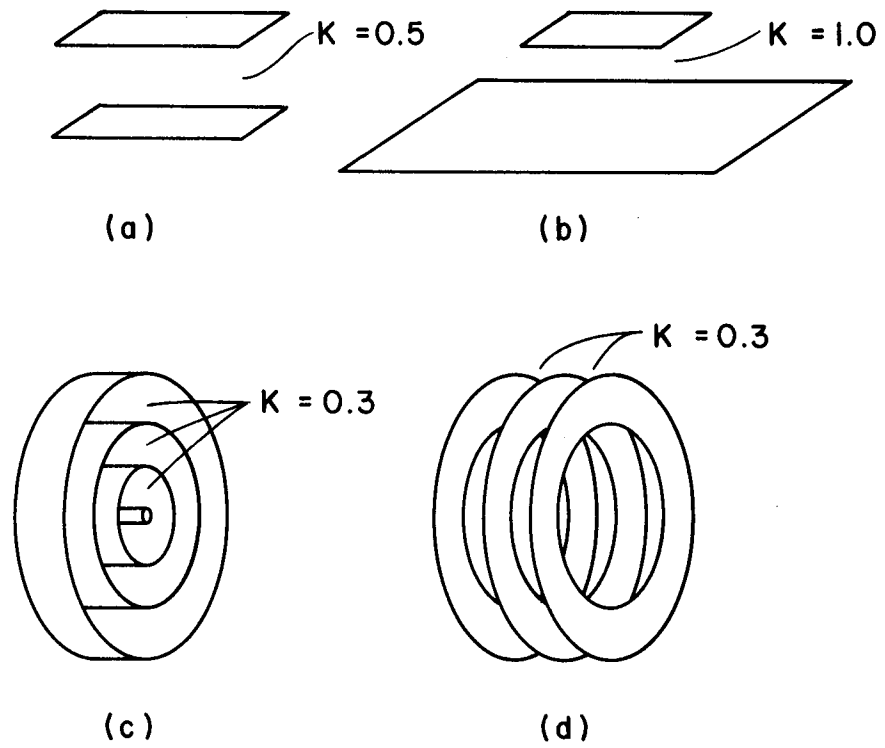
Fig. 14.   Fringe-field constants for several pole-piece configurations.

Design Example

Consider a multipole chamber with a 10 cm inside diameter. The outer wall pole pieces (Fig. 14(d)) are assumed to be 2.5 cm wide and 2.5 cm apart. These particular values were chosen to give adequate space for an anode and insulated supports (including sputter shields). The pole pieces involved should thus have inside and outside diameters of 10 and 15 cm. Also assume that the magnetic integral protecting an anode with a 10 cm inside diameter is desired to be 70×10^{-6} T-m (70 Gauss-cm).

The fringe field in the equivalent field shape, Fig. 13(b), is assumed to be located within 0.3 times the pole-piece spacing, or $0.3 \times 2.5 = 0.75$ cm. For an integral of 70×10^{-6} T-m over 0.75 cm, the field strength must be 0.0093 T. The effective area over which this field must be produced is an annulus with an inside diameter of 8.5 cm (10 – (2 × 0.75)) and an outside diameter of 16.5 cm (15 + (2 × 0.75)). The total flux for this area is $0.0093 \times \pi \ (0.0825^2 - 0.0425^2) = 1.46 \times 10^{-4}$ Webers. The magnet cross-section area to support this flux at a 1 T flux density is simply 1.46×10^{-4} m^2. If the magnets to be used are 6 mm in diameter, the cross-section area of one magnet is 2.83×10^{-5} m^2 and five magnets should be used to approximate the desired total flux. For a 6 mm diameter of permanent magnets, the pole-piece thickness should be $\geq$ 1.5 mm. With a magnet length of ∿25 mm, the minimum length-to-diameter ratio of 4 is also satisfied.

The calculation is similar for the pole pieces at the end of the discharge chamber, Fig. 14(c), except that the anode and the flux density are assumed to be at a mean radius between the two pole pieces of interest. Keep in mind that magnetic circuit calculations can involve large errors. It is generally necessary for the field strength to be measured

and adjustments made after construction. The adjustments made are usually in the strength and/or number of permanent magnets. Again, careful handling of the permanent magnets is essential for predictable performance.

For field measurement, it is at first usually necessary to measure the field strength at enough points to permit numerical calculation of the integral protecting the anode. This integral should show a close relationship to the maximum field strength on a plane midway between the pole pieces. After a few comparisons of the integral and maximum values, the maximum can be used to replace more detailed integral measurements. In the design under consideration, the measured maximum value should be roughly the assumed value of 0.0093 T (93 Gauss) for the desired integral of 70×10^{-6} T-m.

VII. MECHANICAL DESIGN

The general construction of an ion source can be divided into conductors and insulators. For conductors, construction is usually of types 304 and 18-8 stainless steels. If either a higher temperature capability (>500°C) or more resistance to warping is required, Mo, Ta, W, or graphite should be considered. Mo and Ta are readily machined but expensive. W can be very expensive to fabricate. Graphite has limited strength and outgasses badly after exposure to the atmosphere, but it is economical and easily machined. Pole pieces will usually require mild steel or 400 series stainless steel for magnetic properties.

For insulators, machinable glass, quartz, alumina, and boron nitride should be considered. Machinable glass has been introduced only recently, but is easily machined to close tolerances and is useful in the lower temperature applications. Quartz is generally used only as tubing. For general purpose insulators at moderately high temperatures, alumina is the preferred material. If machined green (before firing), allowance must be made for dimensional changes during firing. Stock parts of alumina usually fall in this category, with large dimensional variations. If machined after firing, machining becomes very expensive. Boron nitride is expensive, but easy to machine. It also has fragility and outgassing problems similar to graphite. If required for its high temperature capability, boron nitride should be subjected to only mild electrical stress, if possible. If a high electrical stress is necessary, outgassing should be thorough before the electrical stress is applied.

Special requirements of some of the individual components will be described in the remainder of this section, together with some of the design approaches that have been used. It should be kept in mind that

there is seldom only one satisfactory way to design a machine. The

approach used is consistent with using an ion source that is separate

and distinct from the vacuum chamber walls. This approach permits thin

walls for the ion source and avoids the need for vacuum tight electrical

feedthroughs within the ion source. It also usually results in the

requirement for heat rejection from the source by radiation, but this

has not proved to be a problem in most applications.

Isolators

Unless the propellant supply is to be operated at ion source

potential, it is necessary to provide electrical isolation somewhere

between the propellant supply and the ion source. Only limited tests

have been conducted, but the isolation requirement appears easy to meet

for nonreactive gases.

An isolator for Ar was built and tested using a 3.2 mm inside

diameter alumina tube, with stainless steel tubing inserted into both

ends.[29] Two single segment lengths, ℓ_s in Fig. 15(a), of 7.7 and 18.4

cm were tested, with breakdown voltages in the 400-600 V range for both

over a wide range of gas flow rates and an operating ion source. The

three segment isolator (5.8 cm per segment) showed an average breakdown

voltage per segment of 300 V, or more. The reduced minimum per segment

(300 versus 400 V) is probably due to uneven voltage division between

segments.

The breakdowns were visible as glows within the alumina tube when

they occurred. The stainless-steel tube between the isolator and ion

source was curved and had an internal length to diameter ratio of more

than 140:1. Despite this physical isolation, the breakdown voltages

were several times higher with the ion source not operating. It appears
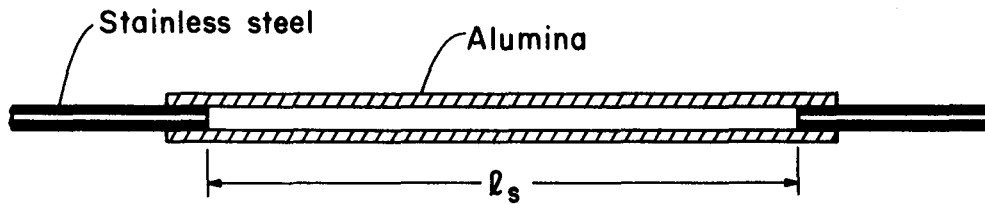
(a)   Single segment configuration
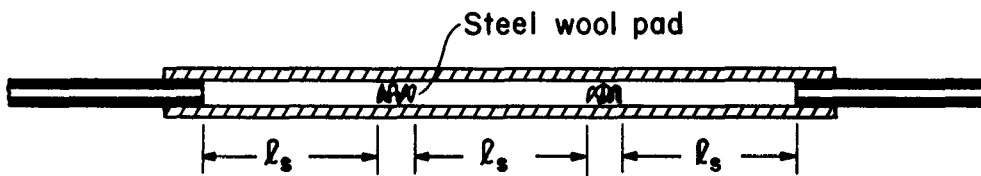
(b)   Multiple segment configuration

Fig. 15. Isolators for ion source gas supply.

clear that some charged particles were traversing the long curved path from the ion source while it was operating. This mobility of charged particles should be kept in mind when designing isolators.

The isolator concept should work well with almost any nonreactive gas. A sufficient number of segments should be provided to assure adequate breakdown voltage. A conservative approach should be to assume the Paschen-law minimum as the avarage per segment (typically 100-300 V). If the gas is condensible (such as Hg), the isolator should, of course, be hot enough to avoid condensation. Much shorter segment lengths than described here were used with Hg, with no apparent adverse effect.

Too high a temperature can cause problems for long-term operation. The combination of electric field stress and temperatures above 300°C was found to result in the surface migration of contaminants and eventual breakdown with Hg gas. If the isolator temperature is low enough, assembly can be simplified by using epoxy cement.

Nonreactive gases have been emphasized in this discussion. As a contrary example, considerable work was done on isolators for Cs in the space propulsion program, with little long-term reliability achieved.

Cathode Support

As mentioned at the beginning of the Mechanical Design section, the approach used does not require vacuum-tight electrical feedthroughs. A typical cathode support assembly, consistent with this approach, is indicated in Fig. 16. The feedthrough insulators and sputter shields are all separate and replaceable in the event of breakage. The only welded or brazed connection is between the torque plate and the long M5 × 0.8 screw. The torque plate and the short screw assembly can be omitted, if desired, but it does serve to keep the long M5 × 0.8 screw
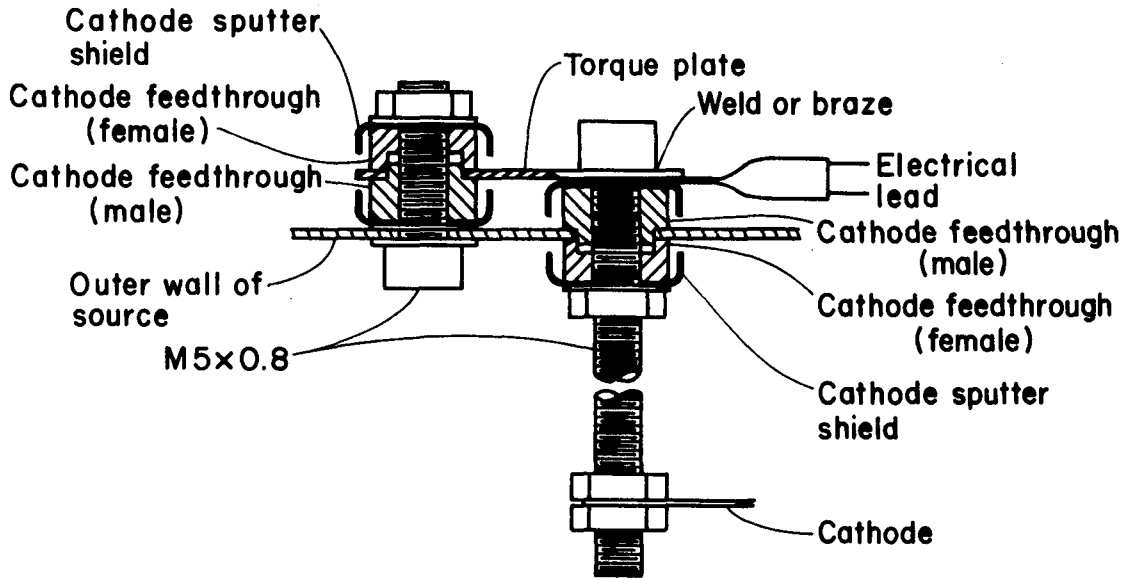
Fig. 16.   Cathode support assembly.

from rotating during cathode replacement. (The M5 × 0.8 designation refers to a metric screw with a nominal 5 mm outside diameter and a 0.8 mm lead. A third number would indicate length in mm.)

Details of the insulators and sputter shields are shown in Figs. 17 and 18. Tolerances on the insulators are sufficient to permit all machining of $\geq 96\%$ pure Al_2O_3 to be before firing. Other notes for insulator fabrication are: break all corners to approximately 0.3 mm radius, runout on flat surfaces is 0.05 mm or less, and cylindrical surfaces coaxial to 0.13 mm or less. A lower purity of Al_2O_3 than 96% can result in a short lifetime due to arcing across the insulator surface.

The sputter shields should be drawn from 0.25 mm thick 304 annealed stainless steel. Low production runs of sputter shields can be accomplished economically with dies in which the material thickness being drawn serves to align and guide the male part of the die.

The cathode support shown in Fig. 16 has been used for heater currents up to 25 A. It may be possible to use this design for higher currents, but there are no data at present to support higher currents. For other screw diameters, scaling laws indicate the same radiation temperature for resistance heating of the screw if the current is varied as the 3/2 power of the screw diameter.

The cathode support design shown in Fig. 16 is intended primarily for the main, or discharge-chamber, cathode. The cathode itself should extend far enough beyond the pole pieces so as to be outside most of the magnetic field, assuming a multipole chamber is used. A distance equal to 1.5-2 times the pole-piece spacing is usually adequate for this purpose. If a small axial-field discharge chamber is used, the cathode should be located near the discharge chamber axis.

Notch depth
and radius,
0.5-0.8

10.8-11.2

5.2-5.5

4.3-4.6

1.4-1.7

7.7-8.0

Inverted

(a) Male

8.2-8.5

1.7-2.0

4.3-4.6

5.2-5.5

10.8-11.2
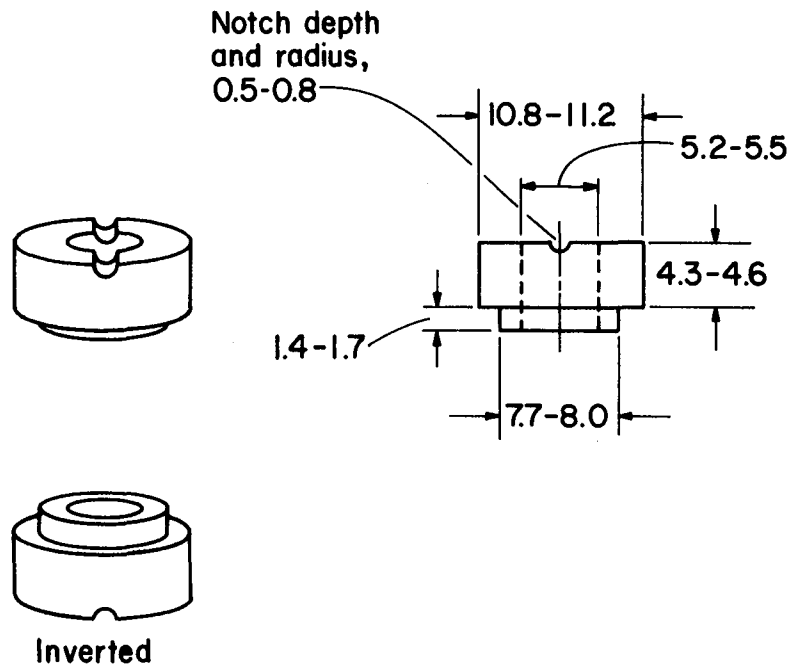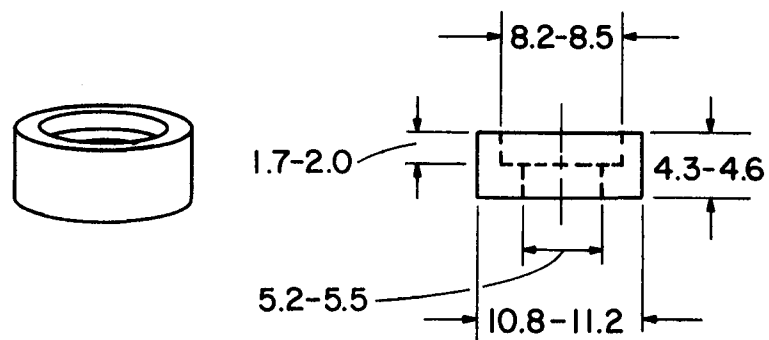
(b) Female

Fig. 17. Cathode feedthrough insulators. (All dimensions in mm.)

Clearance hole
for M5×0.8

Inside radius
approx. 0.8

3.6± 0.2

├──13.8±0.1──┤
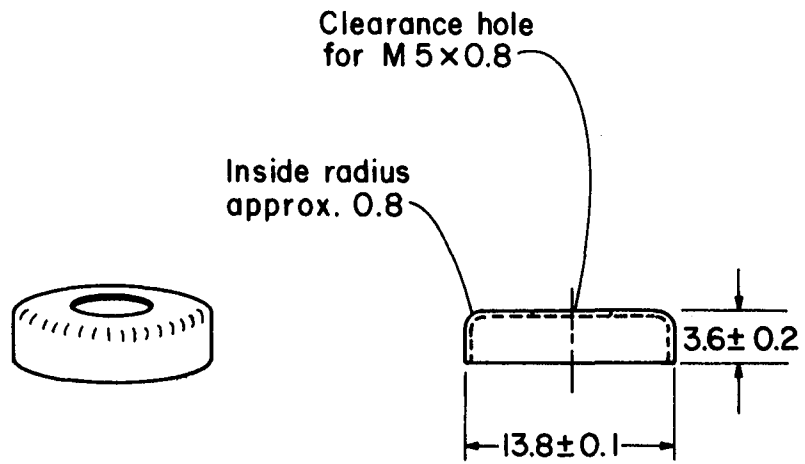
Fig. 18. Cathode sputter shield. (All dimensions in mm.)

Access to the main cathode is usually possible by removing the ion optics. But this can be excessively tedious, as well as risking damage to the relatively delicate optics. The preferred approach is to have the cathode supports attached to a separate plate, which can be dis-mounted for cathode replacement by removing 2-4 screws. Push-on con-nectors are convenient for the associated wiring connections.

The neutralizer can also be supported in a manner similar to that shown in Fig. 16. Because of the exposed location of neutralizers, it is usually not necessary to make special provision for easy access.

Anode Support

A typical anode support is indicated in Fig. 19. The insulators and sputter shields are identical to those used for the cathode support except that the central holes in the insulators are all 3.2-3.5 mm and the holes in the sputter shields are M3 × 0.5 clearance holes.

The pole pieces are assumed to be 25 mm wide and 25 mm apart in Fig. 18. With these dimensions, feedthroughs and sputter shields of the sizes described above will fit with adequate clearances between parts. A U-shaped anode of 0.5 mm thick stainless steel is assumed for Fig. 18. An anode of this shape is excellent for a rectangular source, but inconvenient for a source with a circular cross section. For the latter, a flat section of stainless steel would be recommended, at least 1.5 mm thick for up to a 30 cm source.

Pole-Piece Assembly

A typical assembly of magnets and pole pieces is indicated in Fig. 20. The pole pieces are recessed to hold the magnets in place. (This recessing is usually ignored in calculating the saturation requirement for pole piece thickness.) The magnets for adjacent pairs of pole
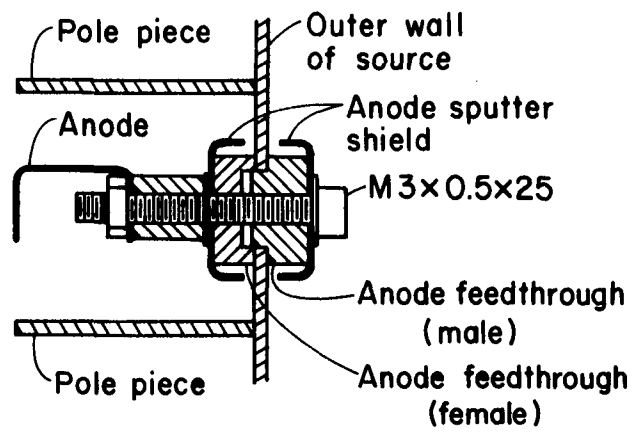
Fig. 19. Anode support assembly.
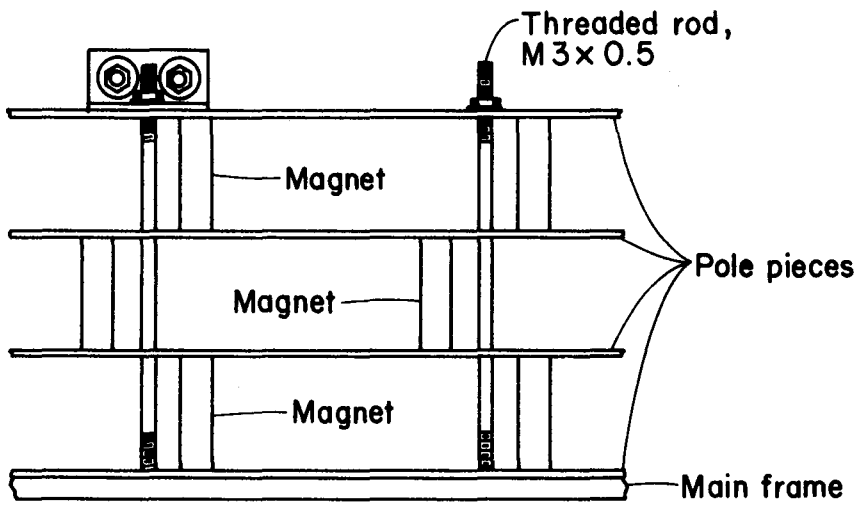
Fig. 20.   Pole-piece assembly.

pieces are offset to avoid doubling the required pole piece thickness. With magnets offset, the structure is less rigid, permitting some compensation for thermal expansion.

Ion Optics

The ion optics usually require the closest tolerances and the most careful design of the entire ion source. A basic concept in the ion optics design is that of span-to-gap ratio, where the gap is the spacing between grids and the span is the beam dimension. For low voltage operation, the smallest possible gap is usually desired to give maximum ion current density. Beyond some rough minimum limit for a given beam diameter, the thermal expansion and warping problems encountered will outweigh any possible performance gain. This minimum gap has been found experimentally to be proportional to the beam diameter for a wide range of design parameters. Some examples of the approximate maximum span-to-gap ratios, d_b/ℓ_g, are given in the following table:

Table 9. Maximum span-to-gap ratios.

Ion-Optics Construction	Max d_b/ℓ_g
Flat Mo	60
Dished Mo	600
Flat graphite	100
Flat pyrolytic graphite*	200

*Oriented with high thermal conductivity and high modulus of elasticity in the plane of the grid.

For rectangular beam grids, the span-to-gap for the short beam dimension should be less than the value given above, since support is provided on only two sides instead of all the way around (as in a circular beam).

In the absence of any further information, the short-dimension span-to-gap ratio is recommended to be half that given in the above table.

For a design example, flat graphite or pyrolytic graphite will be assumed. A rigid flat surface is assumed for mounting the screen grid. The screen should be drawn up against this surface with a sufficient number of screws to prevent buckling due to compressive stresses in the plane of the screen grid. (In the absence of any design details, 8-12 screws should be considered for a 20-30 cm source.) At the same time, these screws should be loose enough to permit relative thermal expansion between the screen grid and the flat surface to which it is mounted. For a mounting surface, a several mm thick plate is recommended for a 10-30 cm source. If the mounting surface is a flange on the end of a cylindrical section, the thickness could be reduced to 1.5-2 mm for the same size source.

There is normally a temperature difference of the order of 100°C between the screen grid and the accelerator grid. With flat grids and a single uniform temperature during ion optics assembly, this temperature difference results in the screen compressive stress mentioned above, together with an accelerator tension stress. If a decelerator is used, the decelerator will be in tension, the screen in compression, and the accelerator at some intermediate stress.

For mounting the accelerator grid to the screen grid, or the decelerator grid to the accelerator grid, the ion optics support assembly shown in Fig. 21 is suggested. The ion-optics insulator is also shown in Fig. 22. All tolerances and fabrication procedures are the same as for the cathode feedthrough, with the exception of the 5.00-5.05 mm dimension, which has to be machined after firing. The groove around the
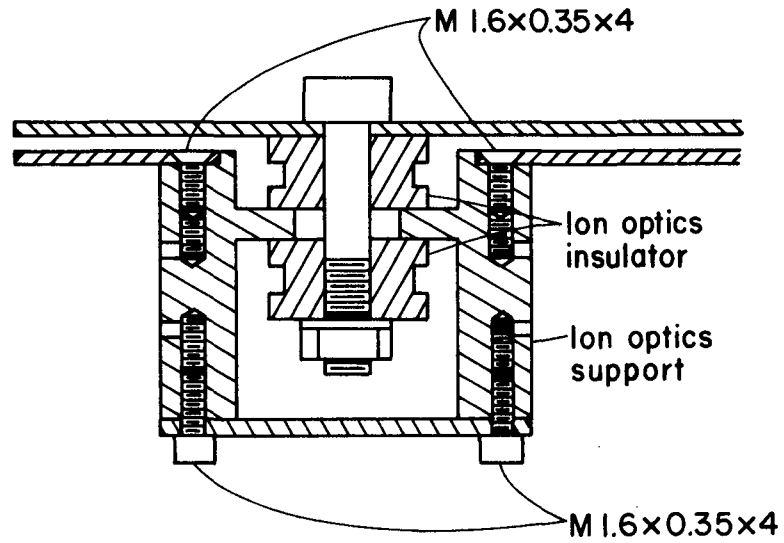
Fig. 21. Ion-optics support assembly.
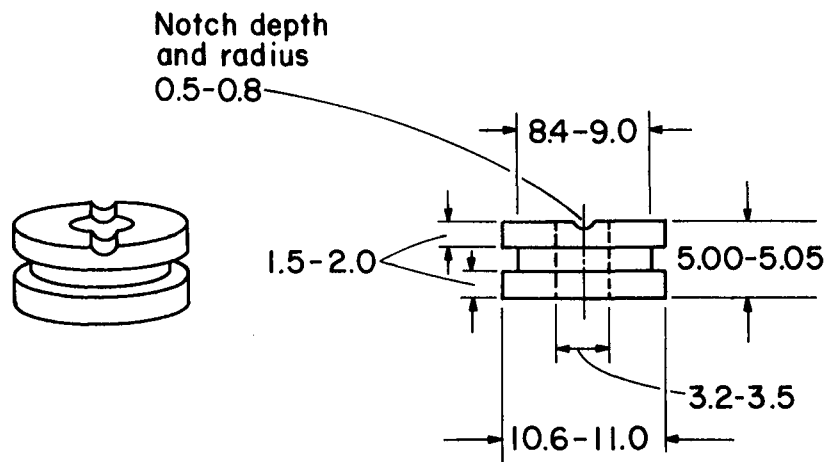
Fig. 22. Ion-optics insulator.

outside of the insulator is not essential, but should reduce the probability of shorting due to sputter deposition of conductor on the insulator.

The ion-optics support is shown in Fig. 23. All dimensions are consistent with a 1 mm grid thickness and a 1 mm gap between grids. The circled numbers in Fig. 23 correspond to the following notes: (1) Two holes drilled and tapped for M1.6 × 0.35 threads, with useful threads at least 4 mm deep. Circumferential locations shown in top view, on 22 mm diameter circle; (2) Four holes drilled and tapped for M1.6 × 0.35 threads, with useful threads at least 4 mm deep. Two circumferential locations shown in top view. Other two hidden behind holes for note (1) in top view, with all four on 22 mm diameter circle; (3) Outgassing holes, 1 mm diameter, to all drilled and tapped holes; (4) Eight out- gassing holes, 1 mm diameter, to center cavity. The material is assumed to be type 304 stainless steel.

As discussed previously, the accelerator grid is in tension relative to the screen grid. (The accelerator grid is less in tension if there is a decelerator grid, but there is still a difference.) Because of this difference in stress and because the screen grid is usually thinner within the beam area, more screen grid mounting screws are required than ion optics supports between grids. For a 20-30 cm diameter beam, 6-8 mounts are suggested. For beam diameters larger than 30 cm, a different mounting design with more accommodation for radial thermal expansion should be considered.

Charge-Exchange-Plasma Shielding

A charge-exchange plasma is generated by a broad-beam ion source, due to the interaction of the beam ions with either the escaping neutrals
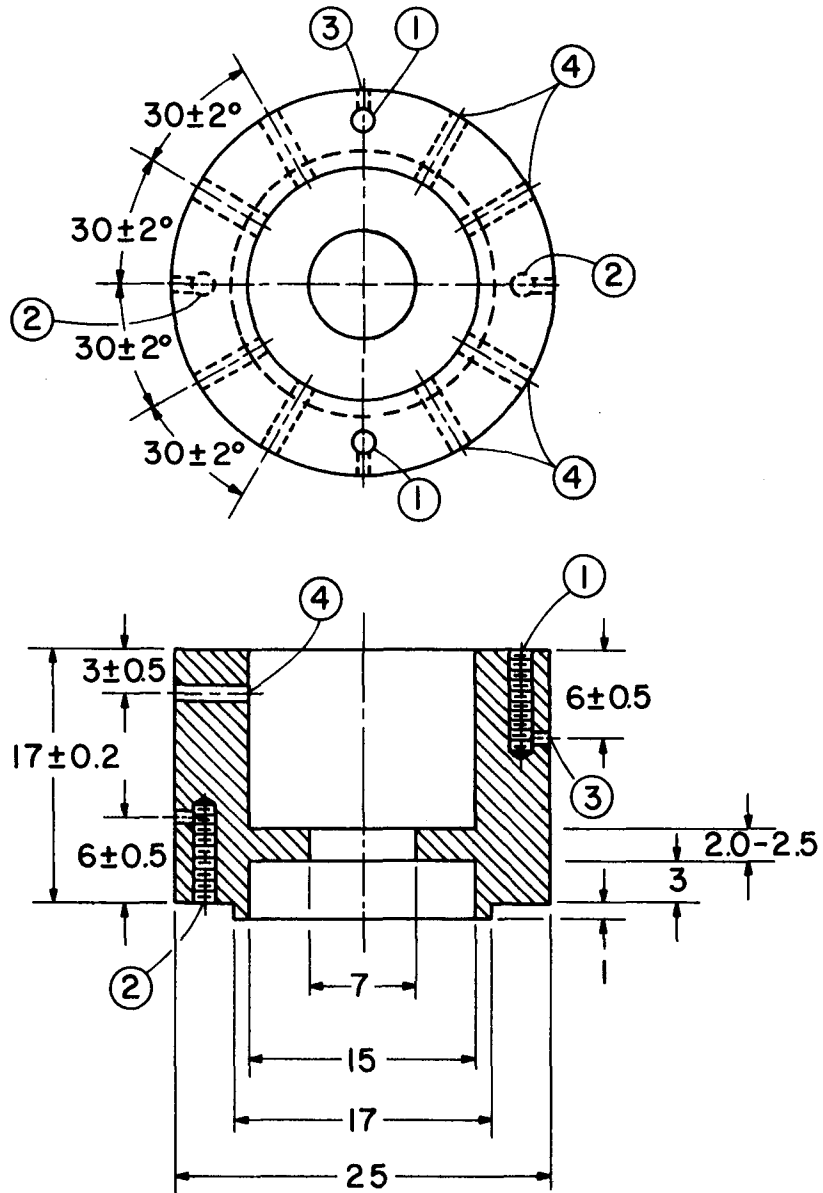
Fig. 23.   Ion-optics support.   (All dimensions in mm.)

or the background gas in the vacuum chamber. This plasma constitutes a low-grade conductor that extends throughout most of the vacuum chamber. Positive electrodes, in particular, tend to draw significant stray electron currents when exposed to this plasma, with the currents often precipitating arcs. To prevent these currents and arcs, it is desirable to shield all positive electrodes.

For positive wires, this covering can be quartz or alumina tubing. To retain flexibility, ceramic beads with interlocking conical ends can also be used. If the temperature and outgassing requirements are moderate, polyimide insulation can be used over standard wire.

For larger electrodes, it is customary to use enclosures in which at least part of the enclosure is perforated or is made of screening – to permit rapid outgassing. The critical parameter in such screening is the size of the apertures. If these apertures are larger than roughly the Debye shielding distance, the plasma will "leak through" a grounded and screened enclosure to reach positive electrodes within. If the apertures are smaller than the Debye distance, the enclosure will effectively behave as a continuous surface with respect to plasma.

The production of a charge-exchange plasma has been worked out for an ion source exhausting into a vacuum.[28] A case of more interest here appears to be the generation of a charge-exchange plasma by an ion beam passing through a neutral background gas of known density. The density may be obtained from an ion gauge (3.29×10^{22} m^{-3} times the pressure in Torr of a 20°C gauge calibration), or it may be calculated using the neutral loss from the discharge chamber if the vacuum-chamber background is negligible.

Assuming an ion beam with a current J_b and a diameter d_b passing through a neutral background gas of density n_o, the production rate for

a charge-exchange cross section σ_{ce} and a beam length L is, for a small

fraction of charge exchange,

$$\dot{N}_{ce} = J_b L n_o \sigma_{ce}/e .$$ (22)

Assuming these charge-exchange ions leave the outer cylindrical surface

of the ion beam with the ion acoustic velocity given by Eq. (1), the

density at this location is

$$n_{ce} = J_b m_i^{1/2} n_o \sigma_{ce}/\pi d_b^{3/2} T_e^{1/2} ,$$ (23)

where T_e is in eV and all other parameters are in SI units. With the

substitution of various constants, this becomes

$$n_{ce} = 2.023 \times 10^{14} J_b m_i^{1/2} n_o \sigma_{ce}/d_b T_e^{1/2} ,$$ (24)

where m_i is now in amu. For further substitution, assume 500 eV Ar^+

ions passing through an Ar neutral background of 10^{-4} Torr, with a beam

diameter of 8 cm and a current density of 1 mA/cm^2. Typical values of 1

eV and 2.3×10^{-19} m^2 for T_e and σ_{ce} then yield

$$n_{ce} = 6.1 \ 10^{14} \times m^{-3} .$$ (25)

Substitution in the equation for the Debye shielding distance then

yields a value of about 0.3 mm. It should be clear that a very fine

mesh will be required to contain the charge-exchange plasma close to the

ion beam. This requirement will ease somewhat with increasing radial

distance from the ion beam and even more behind the ion source, but it
is a basic environmental problem associated with broad beam ion sources.

VIII.   CONCLUDING REMARKS

Design techniques for the various components of broad-beam electron-bombardment sources are presented. These techniques have emphasized simple and easily used concepts, together with numerical examples and drawings of sample designs. These design techniques, numerical examples, and sample designs should be considered as representative of current technology. Used in this manner, they can serve to facilitate rapid development of design skill in this rapidly growing field of broad-beam ion source technology.

REFERENCES

1. E. Stuhlinger, <u>Ion Propulsion for Space Flight</u>, McGraw-Hill Book Co., New York (1964).

2. G. R. Brewer, <u>Ion Propulsion</u>, Gordon and Breach, New York (1970).

3. R. G. Jahn, <u>Physics of Electric Propulsion</u>, Gordon and Breach, New York (1970).

4. H. R. Kaufman, "Technology of Electron Bombardment Ion Thrusters," in <u>Advances in Electronics and Electron Physics, Vol. 36</u> (L. Marton, ed.), Academic Press, New York, pp. 265-373 (1974).

5. H. R. Kaufman, "Technology of Ion Beam Sources used in Sputtering," <u>J. Vac. Sci. Technol.</u>, Vol. 15, pp. 272-276, Mar./Apr. 1978.

6. C. M. Haynes, "Reactive Ion Beam Etching," in <u>NASA Contr. Rep.</u> CR-159877, pp. 2-7, Dec. 1979.

7. J. M. E. Harper, J. J. Cuomo, P. A. Leary, G. M. Summa, H. R. Kaufman, and F. J. Bresnock, "Low Energy Ion Beam Etching," <u>Proc. Symp. Electron and Ion Beam Science and Technol.</u>, <u>Proc. Electrochem. Soc.</u>, Vol. 80-6, pp. 518-530 (1980).

8. R. G. Wilson and G. R. Brewer, <u>Ion Beams, with Applications to Ion Implantation</u>, John Wiley and Sons, New York (1973).

9. J. H. Freeman and G. Sidenius, "The Technology and Chemistry of Heavy Ion Sources," <u>Nucl. Instr. and Meth.</u>, Vol. 107, pp. 447-492, 1973.

10. H. Baumann and K. Bethge, "PIG Ion Source with End Extraction for Multiply Charged Ions," <u>Nucl. Instr. and Meth.</u>, Vol. 122, pp. 517-525, 1974.

11. K. O. Nielsen, "The Development of Magnetic Ion Sources for an Electromagnetic Isotope Separator," <u>Nucl. Instrum.</u>, Vol. 1, pp. 289-301, 1957.

12. I. Chavet and R. Bernas, "Experimental Study of an Ion Source for Electromagnetic Isotope Separation with a View to High Efficiency Operation," <u>Nucl. Instr. and Meth.</u>, Vol. 51, pp. 77-86, 1967.

13. H. R. Kaufman and A. J. Cohen, "Maximum Propellant Utilization in an Electron Bombardment Thruster," in <u>Proc. Symp. on Ion Sources and Formation of Ion Beams</u> (Th. J. M. Sluyters, ed.), pp. 61-68, Brookhaven Nat. Lab., Oct. 1971.

14. T. S. Green, "Intense Ion Beams," in <u>Rep. Prog. Phys.</u>, Vol. 37, pp. 1257-1344, 1974.

15. P. Clausing, Über die Strömung sehr verdünnter Gase durch Rören von beliebiger Länge, <u>Ann. Physik</u>, Vol. 12, pp. 961-989, 1932.

16. H. R. Kaufman and R. S. Robinson, "Plasma Processes in Inert Gas Thrusters," AIAA Paper No. 79-2055, Oct./Nov. 1979.

17. G. Aston and H. R. Kaufman, "The Ion-Optics of a Two-Grid Electron-Bombardment Thruster," AIAA Paper No. 76-1029, Nov. 1976.

18. G. Aston, H. R. Kaufman, and P. J. Wilbur, "Ion Beam Divergence Characteristics of Two-Grid Accelerator Systems," AIAA J., Vol. 16, pp. 516-524, May 1978.

19. H. R. Kaufman, "Accelerator-System Solutions for Electron-Bombardment Ion Sources," AIAA Paper No. 75-430, Mar. 1975.

20. H. R. Kaufman, "Accelerator-System Solutions for Broad-Beam Ion Sources," AIAA J., Vol. 15, pp. 1025-1034, July 1977.

21. L. D. Stewart, J. Kim, and S. Matsuda, "Beam Focusing by Aperture Displacement in Multiampere Ion Sources," Rev. Sci. Instr., Vol. 46, pp. 1193-1196, Sept. 1975.

22. J. H. Whealton, E. F. Jaeger, and J. C. Whitson, "Optics of Single-Stage Accelerated Ion Beams Extracted from a Plasma," Rev. Sci. Instr., Vol. 48, pp. 829-831, July 1977.

23. G. Aston and H. R. Kaufman, "Ion Beam Divergence Characteristics of Three-Grid Accelerator Systems," AIAA Paper No. 78-669, Apr. 1978.

24. G. Aston and H. Kaufman, "Ion Beam Divergence Characteristics of Three-Grid Accelerator Systems," AIAA J., Vol. 17, pp. 64-70, Jan. 1979.

25. H. R. Kaufman, J. M. E. Harper, and J. J. Cuomo, "Focused Ion Beam Designs for Sputter Deposition," J. Vac. Sci. Technol., Vol. 16, pp. 899-905, May/June 1979.

26. W. H. Kohl, Materials and Techniques for Vacuum Devices, Reinhold Publ. Corp., New York, pp. 261, 301, 303, 478, 482 (1967).

27. I. Langmuir, "The Effect of Space Charge and Residual Gases on Thermionic Currents in High Vacuum," Phys. Rev., Ser. 2, Vol. 2, pp. 450-486, 1913.

28. H. R. Kaufman and G. C. Isaacson, "The Interactions of Solar Arrays with Electric Thrusters," AIAA Paper No. 76-1051, Nov. 1976.

29. R. S. Robinson, "Propellant Isolator," in NASA Contr. Rep. CR-135226, pp. 65-69, July 1977.

DISTRIBUTION LIST

National Aeronautics and Space Administration
Washington, DC 20546
Attn: RS/Mr. Dell Williams, III   1
       RTS-6/Mr. Wayne Hudson   1
       RTS-6/Mr. Jerome Mullin   1
       MT/Mr. Ivan Bekey   1

National Aeronautics and Space Administration
Lewis Research Center
21000 Brookpark Road
Cleveland, OH 44135
Attn: Research Support Procurement Section
        Mr. G. Golinski, MS 500-306   1
        Technology Utilization Office, MS 3-19   1
        Report Control Office, MS 5-5   1
        Library, MS 60-3   2
        Mr. N. Musial, MS 500-113   1
        Dr. M. Goldstein, Chief Scientist, MS 5-3   1
        Mr. T. Cochran, MS 501-8   1
        Mr. D. Petrash, MS 501-5   1
        Mr. N. Grier, MS 501-7   1
        Mr. M. Mirtich, MS 501-7   1
        Mr. R. Finke, MS 77-4   1
        Mr. B. Banks, MS 501-7   1
        Mr. D. Byers, MS 501-7   1
        Mr. W. Kerslake, MS 501-7   30

National Aeronautics and Space Administration
Lyndon B. Johnson Space Center
Houston, TX 77058
Attn: Mr. Hu Davis   1

National Aeronautics and Space Administration
Marshall Space Flight Center
Huntsville, AL 35812
Attn: Mr. Jerry P. Hethcoate   1
       Mr. John Harlow   1
       Mr. John Brophy   1
       Mr. Robert T. Bechtel   1

NASA Scientific and Technical
  Information Facility
P.O. Box 8757
Baltimore, MD 21240
Attn: Accessioning Department   1

National Aeronautics and Space Administration
Goddard Space Flight Center
Greenbelt, MD 20771
Attn: Mr. W. Isley, Code 734   1
       Mr. A. A. Vetman   1
       Dr. David H. Suddeth   1

National Aeronautics and Space Administration
Ames Research Center
Moffett Field, CA 94035
Attn: Technical Library   1

National Aeronautics and Space Administration
Langley Research Center
Langley Field Station
Hampton, VA 23365
Attn: Technical Library   1
       Mr. B. Z. Henry   1

The Aerospace Corporation
P.O. Box 95085
Los Angeles, CA 90045
Attn: Dr. B. A. Haatunion   1
       Mr. A. H. Silva   1

The Aerospace Corporation
Space Sciences Laboratory
P.O. Box 92957
Los Angeles, CA 90009
Attn: Dr. Y. T. Chiu   1

Bell Laboratories
600 Mountain Avenue
Murray Hill, NJ 07974
Attn: Dr. Edward G. Spencer   1
       Dr. Paul H. Schmidt   1

Boeing Aerospace Company
P.O. Box 3999
Seattle, WA 98124
Attn: Mr. Donald Grim, MS 8K31   1
       Mr. Russell Dod   1

Case Western Reserve University
10900 Euclid Avenue
Cleveland, OH 44106
Attn: Dr. Eli Reshotko   1

C.E.N.-F.A.R.
Service Du Confinement Des Plasmas
BP6
92260 Fontenay-Aux-Roses,
FRANCE
Attn: J. F. Bonnal   1

Circuits Processing Apparatus, Inc.
725 Kifer Road
Sunnyvale, CA 94086
Attn: Spencer R. Wilder   1

Commonwealth Scientific Corporation
500 Pendleton Street
Alexandria, VA 22314
Attn: George R. Thompson   1

Computing Center of the USSR Academy of Sciences
Vavilova 40
117333 Moscow, B-333
USSR
Attn: Dr. V. V. Zhurin   1

Comsat Corporation
950 L'Enfant Plaza, S.W.
Washington, DC 20024
Attn: Mr. Sidney O. Metzger   1

COMSAT Laboratories
P.O. Box 115
Clarksburg, MD 20734
Attn: Mr. B. Free   1
       Mr. O. Revesz   1

CVC Products
525 Lee Road
P.O. Box 1886
Rochester, NY 14603
Attn: Mr. Georg F. Garfield, Jr.   1

DFVLR - Institut fur Plasmadynamik
Technische Universitat Stuttgart
7 Stuttgart-Vaihingen
Allmandstr 124
WEST GERMANY
Attn: Dr. G. Krulle   1

DFVLR - Institut fur Plasmadynamik
33 Braunschweig
Bienroder Weg 53
WEST GERMANY
Attn: Mr. H. Bessling   1

EG & G Idaho
P.O. Box 1625
Idaho Falls, ID 83401
Attn: Dr. G. R. Longhurst, TSA-104   1

Electro-Optical Systems, Inc.
300 North Halstead
Pasadena, CA 91107
Attn: Dr. R. Worlock   1
       Mr. E. James   1
       Mr. W. Ramsey   1

Electrotechnical Laboratory
1-1-4, Umezono, Sakura-Mura,
Niihari-Gun
Ibaraki,
JAPAN
Attn: Dr. Katsuya Nakayama   1

Fairchild Republic Company
Farmingdale, NY 11735
Attn: Dr. Domenic J. Palumbo   1

Ford Aerospace Corporation
3939 Fabian Way
Palo Alto, CA 94303
Attn: Mr. Robert C. Kelsa   1

General Dynamics
Kearney Mesa Plant
P.O. Box 1128
San Diego, CA 92112
Attn: Dr. Ketchum   1

Giessen University
1st Institute of Physics
Giessen,
WEST GERMANY
Attn: Professor H. W. Loeb   1

Hughes Aircraft Company
Space and Communication Group
P.O. Box 92919
Los Angeles, CA 90009
Attn: Dr. M. E. Ellison   1
       Dr. B. G. Herron   1

Hughes Research Laboratories
3011 Malibu Canyon Road
Malibu, CA 90265
Attn: Mr. J. H. Molitor   1
       Dr. R. L. Poeschel   1
       Dr. Jay Hyman   1
       Mr. R. Vahrenkamp   1
       Dr. J. R. Beattie   1
       Dr. W. S. Williamson   1

IBM Corporation
Thomas J. Watson Research Center
P.O. Box 218
Yorktown Heights, NY 10598
Attn: Dr. Jerome J. Cuomo   1
       Dr. James M. E. Harper   1

IBM East Fishkill
D/42K, Bldg. 300-40F
Hopewell Junction, NY 12533
Attn: Mr. James Winnard   1

Ion Beam Equipment, Inc.
P.O. Box O
Norwood, NJ 07648
Attn: Dr. W. Laznovsky   1

Ion Tech, Inc.
P.O. Box 1388
1807 E. Mulberry
Fort Collins, CO 80522
Attn: Dr. Gerald C. Isaacson   1

Jet Propulsion Laboratory
4800 Oak Grove Drive
Pasadena, CA 91102
Attn: Dr. Kenneth Atkins   1
       Technical Library   1
       Mr. Eugene Pawlik   1
       Mr. James Graf   1
       Mr. Dennis Fitzgerald   1
       Dr. Graeme Aston   1

Joint Institute for Laboratory Astrophysics
University of Colorado
Boulder, CO 80302
Attn: Dr. Gordon H. Dunn   1

Kirtland Air Force Base
Office of Assistant for Study Support
Albuquerque, NM 87117
Attn: Dr. Berhart Eber OAS Ge   1

Kyoto University
The Takagi Research Laboratory
Department of Electronics
Yoshidahonmachi Sakyo-ku
Kyoto 606,
JAPAN
Attn: Dr. Toshinori Takagi   1

Lawrence Livermore Laboratory
Mail Code L-437
P.O. Box 808
Livermore, CA 94550
Attn: Dr. Paul Drake   1

Lockheed Missiles and Space Company
Sunnyvale, CA 94088
Attn: Dr. William L. Owens
       Propulsion Systems, Dept. 62-13   1
       Mr. Carl Rudey   1

Marshall Spaceflight Center
Huntsville, AL 35812
Attn: M. Ralph Carruth, Jr., MS EC35   1

Massachusetts Institute of Technology
Room 13-3061
77 Massachusetts Avenue
Cambridge, MA 02139
Attn: Henry I. Smith   1

New Mexico State University
Department of Electrical and Computer Engr.
Las Cruces, NM 88003
Attn: Dr. Robert McNeil   1

Optic Electronics Corporation
11477 Pagemill Road
Dallas, TX 75243
Attn: Bill Hermann, Jr.   1

Physicon Corporation
221 Mt. Auburn Street
Cambridge, MA 02138
Attn: H. von Zweck   1

Princeton University
Princeton, NJ 08540
Attn: Mr. W. F. Von Jaskowsky   1
       Dean R. G. Jahn   1
       Dr. K. E. Clark   1

Research and Technology Division
Wright-Patterson AFB, OH 45433
Attn: (ADTN) Mr. Everett Bailey   1

Rocket Propulsion Laboratory
Edwards AFB, CA 93523
Attn: LKDA/Mr. Tom Waddell   1
       LKDH/Dr. Robert Vondra   1

Royal Aircraft Establishment
Space Department
Farnborough, Hants
ENGLAND
Attn: Dr. D. G. Fearn   1

Sandia Laboratories
Mail Code 5743
Albuquerque, NM 87115
Attn: Mr. Ralph R. Peters   1

Tektronix, 50-324
P.O. Box 500
Beaverton, OR 97077
Attn: Curtis M. Haynes   1

Texas Instruments, Inc.
MS/34
P.O. 225012
Dallas, TX 75265
Attn: Larry Rehn   1

TRW Inc.
TRW Systems
One Space Park
Redondo Beach, CA 90278
Attn: Dr. M. Huberman   1
       Mr. H. Ogawa   1
       Mr. Sid Zafran   1

United Kingdom Atomic Energy Authority
Culham Laboratory
Abingdon, Berkshire
ENGLAND
Attn: Dr. P. J. Harbour   1
       Dr. M. F. A. Harrison   1
       Dr. T. S. Green   1

University of Tokyo
Department of Aeronautics
Faculty of Engineering
7-3-1, Hongo, Bunkyo-ku
Tokyo,
JAPAN
Attn: Prof. Itsuro Kimura   1

Veeco Instruments, Inc.
Terminal Drive
Plainview, NY 11803
Attn: Norman Williams   1